sustainability

MDPI

Article

Peplospheric Influences on Local Greenhouse Gas and Aerosol Variability at the Lamezia Terme WMO/GAW Regional Station in Calabria, Southern Italy: A Multiparameter Investigation

Francesco D'Amico [1,2,*], Claudia Roberta Calidonna [1], Ivano Ammoscato [1], Daniel Gullì [1], Luana Malacaria [1], Salvatore Sinopoli [1], Giorgia De Benedetto [1] and Teresa Lo Feudo [1,*]

[1] Institute of Atmospheric Sciences and Climate, National Research Council of Italy, Area Industriale Comp. 15, I-88046 Lamezia Terme, Catanzaro, Italy; claudiaroberta.calidonna@cnr.it (C.R.C.); i.ammoscato@isac.cnr.it (I.A.); d.gulli@isac.cnr.it (D.G.); l.malacaria@isac.cnr.it (L.M.); s.sinopoli@isac.cnr.it (S.S.); g.debenedetto@isac.cnr.it (G.D.B.)

[2] Department of Biology, Ecology and Earth Sciences, University of Calabria, Via Bucci Cubo 15B, I-87036 Rende, Cosenza, Italy

* Correspondence: f.damico@isac.cnr.it or francesco.damico@unical.it (F.D.); t.lofeudo@isac.cnr.it (T.L.F.)

Abstract: One of the keys towards sustainable policies and advanced air quality monitoring is the detailed assessment of all factors that affect the surface concentrations of greenhouse gases (GHGs) and aerosols. While the development of new atmospheric tracers can pinpoint emission sources, the atmosphere itself plays a relevant role even at local scales: Its dynamics can increase, or reduce, surface concentrations of pollutants harmful to human health and the environment. PBL (planetary boundary layer), or peplospheric, variability is known to affect such concentrations. In this study, an unprecedented characterization of PBL cycles and patterns is performed at the WMO/GAW regional coastal site of Lamezia Terme (code: LMT) in Calabria, Southern Italy, in conjunction with the analysis of key GHGs and aerosols. The analysis, accounting for five months of 2024 data, indicates that peplospheric variability and wind regimes influence the concentrations of key GHGs and aerosols. In particular, PBLH (PBL height) patterns have been tested to further influence the surface concentrations of carbon monoxide (CO), black carbon (BC), and particulate matter (PM). This research introduces four distinct wind regimes at LMT: breeze, not complete breeze, eastern synoptic, and western synoptic, each with its peculiar influences on the local transport of gases and aerosols. This research demonstrates that peplosphere monitoring needs to be considered when ensuring optimal air quality in urban and rural areas.

Keywords: Lamezia Terme; GAW; sustainability; peplosphere; planetary boundary layer; atmospheric boundary layer; Mediterranean basin; greenhouse gas; aerosol; synoptic flow

Citation: D'Amico, F.; Calidonna, C.R.; Ammoscato, I.; Gullì, D.; Malacaria, L.; Sinopoli, S.; De Benedetto, G.; Lo Feudo, T. Peplospheric Influences on Local Greenhouse Gas and Aerosol Variability at the Lamezia Terme WMO/GAW Regional Station in Calabria, Southern Italy: A Multiparameter Investigation. *Sustainability* **2024**, *16*, 10175. https://doi.org/10.3390/su162310175

Academic Editors: O. V. Giannico, Roberta Zupo and Maria Lisa Clodoveo

Received: 16 October 2024
Revised: 17 November 2024
Accepted: 18 November 2024
Published: 21 November 2024

1. Introduction

The peplosphere, also referred to in the literature as the planetary boundary layer (PBL) or atmospheric boundary layer (ABL), is the lowest part of the atmosphere. The peplosphere is heavily influenced in its dynamics by constant contact with Earth's surface [1–6]; it is also characterized by turbulences, vertical currents, distinct temperature profiles, and air flows, which are not parallel to the surface or isobars [7–10]. Only in the free atmosphere above, air flows are mostly geostrophic [11,12].

The peplosphere has a well-defined diurnal–nocturnal cycle [13–19], which also results in peculiar dynamics directly affected by this cycle [20–24]. PBLH (planetary boundary layer height) is among the key parameters used in research to characterize peplospheric variability over time [25–27]. The PBLH is normally described as the height of the inversion level separation between the free troposphere above the boundary layer [14]. In addition to the physical boundary of the peplosphere, it is worth mentioning that it possesses peculiar characteristics in terms of microbial ecology [28,29].

Research demonstrated correlations between PBLH and the concentration of several GHGs and aerosols: Therefore, peplospheric control over the surface concentration of these compounds is among the factors that can help predict their variability and diffusion [30–37]. This also has a number of implications in terms of human health and environmental protection, as higher concentrations can lead to hazards [38–40]. For example, in the case of black carbon (BC), an inverse correlation with PBLH was demonstrated in areas affected by anthropogenic pollution [41]. In a world that is constantly dealing with climate change, air quality issues, and the need for sustainable policies and regulations [42], additional knowledge on the peplosphere may be required.

In research, two main methods for PBLH measurement are used: the gradient method and the threshold method. The former estimates PBLH by pinpointing the height of the minimum backscatter gradient [43–47], while the latter estimates PBLH as the threshold at which the backscatter signal is below a certain value [45,48].

In addition to the complexities of surface-peplosphere-free atmosphere interactions that normally occur on Earth, a significant role in peplospheric dynamics is played by the presence of sea/ocean masses, continents, and coastal boundaries below [8,49–56]. These extra complexities require ad hoc methodologies to assess PBLH variability in these environments [57–59]. A better understanding of peplospheric influences over the concentration of GHGs and aerosols is necessary to provide regulators and policymakers with additional tools to better manage air quality issues in urban and rural areas. Various parameters affect air quality and local air pollution; this research paper will focus on three gases and two aerosol types.

Carbon dioxide (CO_2) is the main driver of present-day anthropogenic climate change [60–62] and is therefore subject to monitoring on local to global scales [63,64]. Although CO_2 does not pose the same health hazards as other pollutants, this compound can impact the environment [65,66] and trigger long-term effects on human health [67–69]. Fossil fuel burning is the main source of anthropogenic CO_2 in the atmosphere [70].

Carbon monoxide (CO) is an effective tracer of combustion and can be both natural and anthropogenic in origin. Wildfires are a prominent source of CO in the atmosphere [71] and the multi-year variability of this gas has shown a generally downward trend [72] that followed years of constant increases [73]. However, the decrease rate of CO has reduced in the past few years, indicating changes in the total global budget [74]. Although carbon monoxide is short-lived, it is known to play a role in the increase of methane [75] and surface ozone (O_3) [76]. CO per se is not defined as a GHG; however, for the sake of convenience, this paper will report it among the GHGs.

Methane (CH_4) is heterogeneous in origin, with anthropogenic [77,78] and natural [79] sources contributing to its global budget. It is also a byproduct of fuel combustion [80,81]. Due to its high GWP (global warming potential) compared to CO_2, CH_4 emission reductions are one of the main challenges of present-day climate change mitigation [82].

Black carbon (BC) is a notable byproduct of combustion processes [71] and acts as both a driver of climate change [83–85] and a factor of health hazard [86]. Its effects are partially counterbalanced by a short persistence rate in the atmosphere: BC has in fact been observed to last for days [87,88].

Particulate matter (PM) is a common byproduct of vehicular emissions in urban areas [89,90] but can also originate from several natural processes [91–93]. PM constitutes a significant health hazard due to its small size and the consequent capacity to affect the lungs directly [94,95]; for this reason, it is subject to constant monitoring at various levels [96]. Several research studies have reported significant correlations between peplospheric and particulate patterns, thus showing that research on PBLH variability has implications for air quality and the sustainable development of urban and rural areas [97–101].

The analyzed parameters are heterogeneous in characteristics, sources, and variability, and the influence of anthropic activities on their release and diffusion is also heterogeneous. The possibility of combining PBLH data with gas and aerosol concentrations, their cycles, and trends further contributes to a better understanding of the local environment.

Previous research aimed at the WMO/GAW (World Meteorological Organization—Global Atmosphere Watch) observation site of Lamezia Terme (code: LMT) in the southern Italian region of Calabria was limited to data gathered during a summer 2009 campaign (12 July to 6 August) [102]. The campaign allowed the characterization of the main features of peplospheric variability at LMT; however, at the time, there were no measurements of GHGs and aerosols available. Further characterization of peplospheric influences over the concentration of pollutants focused on the 2015 solar eclipse [103], but the study could not provide additional details on variability over time.

This study is therefore aimed at an unprecedented analysis of PBLH variability at LMT, as well as its correlations with the patterns of key GHGs and aerosols, via the implementation of additional instruments and data that were not available during the short 2009 campaign. Specifically, this research paper is targeted at further characterization of LMT in the context of Mediterranean observation sites. This paper is divided as follows: Section 2 describes the LMT site, its instruments, and datasets; Section 3 will show the results of this campaign; Sections 4 and 5 cover the discussion and results, respectively.

2. The Station, Methods, Instruments, and Datasets

2.1. The Observation Site and Its Characteristics

Fully operated by the National Research Council of Italy—Institute of Atmospheric Sciences and Climate (CNR-ISAC), the observation site (code: LMT; Lat: 38.88 N°; Lon: 16.23 E°; Elev: 6 m.a.s.l.) is located in the southern Italian region of Calabria, in the municipality of Lamezia Terme (Figure 1). The station is located 600 m from the Tyrrhenian coast of the region, in an area known to be the narrowest point in the entire Italian peninsula, as the distance between the Tyrrhenian and Ionian coasts is ≈30 km. This area, known as the Catanzaro isthmus, effectively separates the coastal chain (*Catena Costiera*) and Sila Massif in the north, from the Serre Massif in the south. The presence of two seas, with the Calabria region in between, leads to increased meteorological instability and oftentimes results in the occurrence of floods in the area [104–106]. Local wind circulation patterns in the western part of the isthmus were characterized in two 2010 studies by Federico and collaborators, who demonstrated the presence of a well-defined west–east local circulation [107,108]. In fact, the Lamezia Terme International Airport (IATA: SUF; ICAO: LICA), located 2 km north of the LMT observatory, has a 10/28 (100/200° N) runway (RWY) orientation and local air traffic is subject to the same wind regime. Vertical wind profiles were characterized in a consequent study [109], which integrated previously gathered data on preliminary peplosphere characterization at the site [102]. A cross-study on multiple southern Italian stations also performed a PBLH characterization via WRF modeling and related methodologies; however, the study was limited to one month of data from the 2009 summer season and did not evaluate GHGs or aerosols [110].

Measurements of GHGs and other key parameters at the site started in 2015. The first study evaluating the results, Cristofanelli et al. (2017) [111], provided new insights into the characterization of LMT and what would later be defined as a "multisource" site. The study also indicated that local wind circulation patterns, characterized in earlier studies [107,108], have a direct influence on LMT observations: Western-seaside winds generally yield low concentrations, while northeastern-continental winds are linked with higher mole fractions of GHGs. With respect to aerosols, a more detailed description was performed in a study by Donateo et al. (2018) [112].

Seven years (2016–2022) of methane data at LMT have been evaluated by D'Amico et al. (2024a) [113] and confirmed the influence of wind regimes on CH_4 mole fractions with additional details. The study also provided new insights on seasonal cycles: The highest mole fractions were observed during the winter season, while the lowest were typically observed during the summer. The authors also found evidence of an HBP (hyperbola branch pattern), with the highest mole fractions linked to low wind speeds and, vice versa, the lowest fractions linked to high speeds. The research by D'Amico et al. (2024d) [114] on nine years (2015–2023) of surface ozone (O_3) data, however, demonstrated that these

patterns do not apply to all parameters, as ozone maxima are linked to spring/summer diurnal winds from the western sector. The presence of opposite or "reversed" patterns at LMT underlined the growing complexity of parameters and how they combine with local wind circulation.

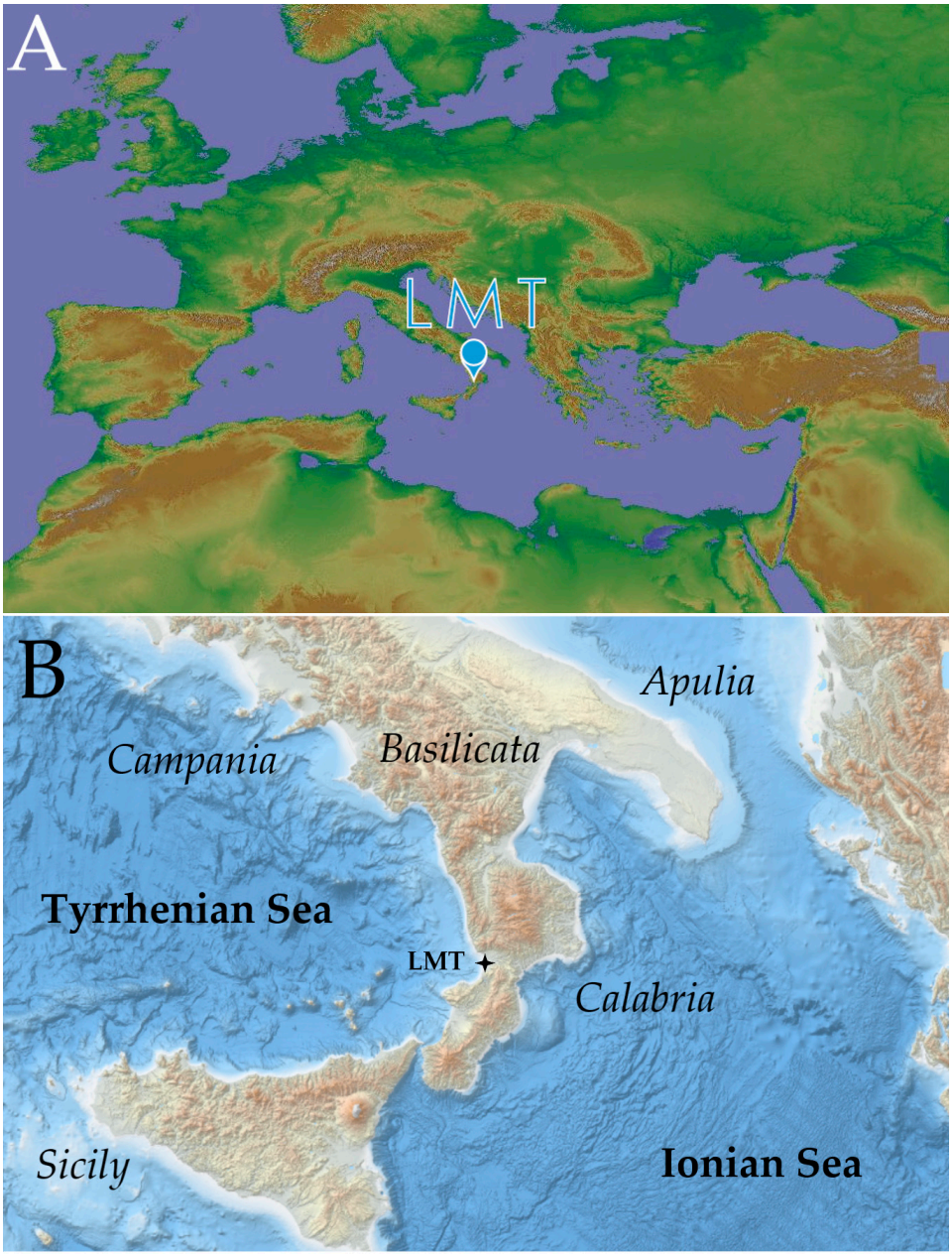

Figure 1. *Cont.*

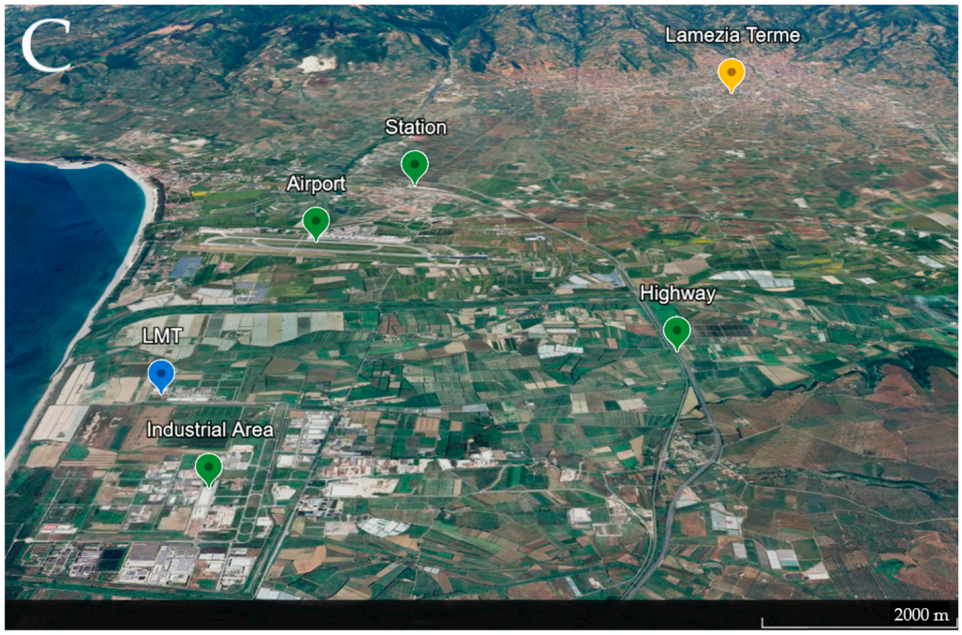

Figure 1. (**A**) Modified Copernicus Digital Elevation Model [115] of Europe, with a mark on LMT's location. (**B**) Modified EMODnet [116] highlighting LMT's specific location in Southern Italy, within the region of Calabria. (**C**) Google Earth map, tilted by 70°, showing the observation site and key infrastructural/emission hotspots in the area. The "Highway" label indicates a point where the distance between LMT and the highway is ≈4.2 km. The "Lamezia Terme" label points to the town center. The "Station" label points to the busiest train station in the municipality of Lamezia Terme, the central one (*Lamezia Terme Centrale*).

During LMT's observational history, a number of local sources of local pollution have been reported as responsible for certain peaks. The international airport located nearby, as well as the A2 highway (part of European route E45), and local livestock farming have been indicated as local sources of methane and other gases in Cristofanelli et al. (2017) [111]. The study also reported possible influence from Tyrrhenian shipping, as the Gioia Tauro port located 60 km southwest of LMT could contribute to pollution in the area. In D'Amico et al. (2024a) [113], the Lamezia Terme central station (*Lamezia Terme Centrale*) was also indicated as a local emission source. Overall, considering its position in central Calabria, Lamezia Terme serves as a transportation hub for the region, with the highway, airport, and central station connecting cross-country Tyrrhenian lines with Ionian lines via an interchange at the Catanzaro isthmus. In Figure 1C, the main sources of anthropogenic pollution in the area are indicated. Farms—including those dedicated to livestock—as well as minor landfills, are spread over the plain.

Research studies on LMT data also focused on weekly trends under the assumption that they can only be anthropic in nature, unlike natural trends characterized by daily, seasonal, and yearly cycles. In D'Amico et al. (2024c) [117], the first COVID-19 lockdown period of 2020 was used to further assess local sources in a context of exceptionally limited anthropic activities due to the strict measures applied by the Italian government to counter the pandemic. In fact, the restrictions introduced at the time [118] preceded similar measures issued by other European countries by days or even weeks, thus allowing changes in LMT data to be linked to local changes in emission sources. A cross-study on aerosol data from multiple southern Italian stations, LMT included, was performed by Donateo et al. (2020) [119] and provided new insights on local vehicular traffic influences on local aerosol diffusion. A more detailed assessment of weekly patterns was performed by D'Amico et al. (2024b) [120] and demonstrated different behaviors of GHGs and aerosols, possibly linked to changes in anthropogenic activities throughout the week. Due to LMT's location in the

central Mediterranean sector, observations are also known to be affected by Saharan dust events [121] and open fires [122].

2.2. Instruments, Methodologies, and Datasets

To retrieve the aerosol backscatter profiles at the monitoring site, a Lufft CHM 15k Nimbus ceilometer (Fellbach, Germany) operating within ALICEnet (Italian Automated LIdar–CEilometer network) was used. The network is coordinated by CNR-ISAC in partnership with other Italian research institutions and environmental agencies. ALICEnet measurements are currently employed to detect the altitude and temporal evolution of cloud layers and track the transport of polluted or mineral dust aerosol plumes at different sites along the Italian peninsula. This ceilometer is a ground-based, monostatic, active remote sensing instrument based on the LiDAR (Light Detection and Ranging) technique and principle [123].

The Nimbus ceilometer observes backscattered profiles with a vertical resolution of 15 m over 24 continuous hours per day. Data are averaged every 15 s. The operating range is between the surface (~15 m) and 15,000 m. Technical details of the instrument are shown in Table 1.

Table 1. Technical specifications of the Lufft CHM 15k Nimbus ceilometer.

Parameters	Description/Values
Laser source	Nd: YAG solid-state laser
Wavelength	1064 nm
Operating mode	Pulsed
Pulse energy	7 µJ
Pulse repetition frequency	5–7 kHz
Filter bandwidth	1 nm
Field of view receiver	0.45 mrad

Specifically, the LiDAR technique is used by the Nimbus to emit short light pulses facing directly upward. Cloud layers, precipitations, and aerosols present in the column scatter back the pulses: By analyzing flight time, the intensity of backscattering, and counted pulses, the main features of the vertical column can be determined. The output is used to evaluate PBLH influences on tropospheric GHG and aerosol transport and dispersion [124]. In particular, the topmost aerosol layer detected by ceilometer pulses and consequent backscatter is used to infer details on PBLH [125]. The expression used to receive the normalized backscattered signal power is reported below (Equation (1)) and is also provided by the manufacturer [126]:

$$P(r) = \frac{P_{raw}(r) - b}{c_s O(r)} \frac{1}{P_{calc}} \quad (1)$$

where $P(r)$ is the normalized backscattered signal power, P_{raw} is the raw backscattered profile (photon counts), b is the baseline, C_s is the calibration constant, $O(r)$ is the overlap function, and P_{calc} is average test pulse intensity. In this study, the beta_raw = $P(r) \times r^2$ output has been used, and negative signals have been filtered out.

During diurnal time ranges, dense and/or multiple cloud and aerosol layers may alter the backscattering signal and generate noise due to attenuation. In order to optimize the accuracy of results, backscattering profile data are averaged on a 5 min basis to improve the signal-to-noise ratio. Raw LIDAR backscatter data are smoothed to reduce noise while preserving signal gradients. Boundary layer height detection is achieved by analyzing variations in backscatter gradients: Significant changes in backscattering indicate layer transitions, such as the peplosphere's topmost layer, and the Gradient Method was used to determine and assess this information. The Gradient Method, as described in Section 1, has its fundament in the calculation of the vertical gradient parameter, which is the first derivative—with respect to height—of the backscatter signal [43–47]. As a derivative, the

gradient is an indicator of the backscatter rate of change; considering that the peplosphere is generally characterized by a higher aerosol concentration compared to the free atmosphere above, backscatter signals would significantly drop at the transition, thus resulting in distinct gradient values. The analysis of peaks and certain thresholds are both used to determine the extent of these transitions [47–49,55].

The campaign took place between May and September 2024, during the boreal warm season: In order to reduce the influence of rainy days, the analysis relied on additional flags used by the Nimbus ceilometer to filter out entire days affected by rain and major cloud covers. This procedure ensured ceilometer data used in this work matched nearly clear sky conditions.

In addition to ceilometer outputs, additional data have been gathered and processed to assess correlations between PBLH, GHGs, pollutants, and key meteorological parameters. All data have been aggregated on an hourly and daily basis to allow direct comparison between different parameters.

Particulate matter (PM) data in micrograms per cubic meter ($\mu g/m^3$ or µg PCM) have been gathered by a Palas Fidas 200 S (Karlsruhe, Germany). The instruments provide both Cn (particle numbers) and PM concentrations; however, in this study, only the latter have been used. A Sigma-2 sampling head draws in ambient air with a flow rate of approximately 0.3 m^3/h. Aerosol gathered from ambient air passes through the sampling tube, equipped with a drying section meant to prevent measurement distortion attributable to moisture particles, and is ultimately drawn by the aerosol sensor. Via a Lorenz-Mie light analysis, particle size is determined by the instrument. Particles move through an optically differentiated volume that is illuminated by a polychromatic LED source. In response, each particle emits an impulse of scattered light that is detected by the instrument at angles of 85 to 95 degrees. Measurements are performed every ≈5 s, and the results have been aggregated on an hourly and daily basis, differentiated by particle size.

Data on downward solar radiation in watts per square meter (W/m^2) have been gathered by a Kipp and Zonen radiometer, model CNR4. The radiometer used at LMT relies on two pyrgeometers and two pyranometers to measure upward (LW, 4.5–42 µm) and downward (SW, 0.31–2.8 µm) irradiance. The uncertainty in CNR4 measurements, traced to the BSRN (Baseline Surface Radiation Network) standard, is approximately 1% [127]. Additional details are available in Lo Feudo et al. (2015) [128] and Romano et al. (2017) [103].

Carbon monoxide (CO), carbon dioxide (CO_2), and methane (CH_4) mole fractions in ppm (parts per million) have been gathered by a Picarro G2401 (Santa Clara, CA, USA) CRDS (Cavity Ring-Down Spectrometry) analyzer [129]. Via the principle of CRDS, these carbon compounds in the atmosphere are measured with high degrees of precision (1 ppb for measurements having an interval of 5 s). At LMT, the G2401 gathers continuous data and is subject to WMO-compliant calibration cycles and procedures. Additional details on G2401 data gathering, calibration procedures, and quality assurance are available in Cristofanelli et al. (2017) [111], D'Amico et al. (2024a) [113], D'Amico et al. (2024b) [120], and D'Amico et al. (2024c) [117].

Key meteorological surface data have been gathered by a Vaisala WXT520 (Vantaa, Finland). The instrument relies on ultrasounds to monitor wind direction and speeds and a transducer to gather temperature data. The WXT520 also gathers data on relative humidity (RH, as a percentage). Temperature is measured with a precision of 0.3 °C, while wind speed and direction are measured with a precision of 0.3 m/s and 3 degrees, respectively. Additional details on WXT520 measurements at Lamezia Terme are available in D'Amico et al. (2024a) [113].

Equivalent black carbon (eBC) micrograms per cubic meter ($\mu g/m^3$ or µg PCM) have been measured by a Thermo Scientific 5012 (Franklin, MA, USA). The instrument operates as a MAAP (Multi-Angle Absorption Photometer), measuring the short-wave absorption parameters of aerosol [130–132]. Specifically, the aerosol absorption coefficient (sa) and equivalent black carbon are measured at 637 nm. The minimum detection of these

measurements is in the <100 ng/m^3 range. Additional details are available in Calidonna et al. (2020) [121], D'Amico et al. (2024b) [120], and D'Amico et al. (2024c) [117].

Particle scattering and hemispheric backscattering coefficients at wavelengths of 450, 525, and 635 nanometers (nm) were measured by an LED-based integrating nephelometer (model Aurora 3000, Ecotech—Knoxfield, Australia) [133] at a temporal resolution of 1 min. Air sampling was obtained from the top of a stainless steel tube having a 15 mm internal diameter and a length of ≈1.5 m. The inlet was fitted with a funnel covered by a screen to prevent raindrops and arthropods from reaching the sample line. No aerosol size cut-off was applied to the sampled air, and a relative humidity threshold of 60% was set by a processor-controlled automatic heater inside the nephelometer to prevent the hygroscopic effects that enhance particle scattering. The reported bandwidth FWHM (Full Width at Half Maximum) of the instrument is 30 nm for 450 and 635 nm wavelengths and 40 nm for the 525 nm wavelength. Calibration data, reported by the instrument under an "AB" status flag, have been excluded from the evaluation.

Each instrument and its respective dataset have been processed and quality-checked. Data coverage rates (%) compared to the actual number of days (153) and hours (3672) elapsed between 1 May 2024 and 30 September 2024 are shown in Table 2.

Table 2. Dataset coverage as a percentage (%) of the total number of days and hours. Coverage variations between instruments are due to maintenance, with the exception of the Nimbus ceilometer whose coverage rate is due to data filtering.

Type	G2401	MAAP	Fidas	WXT520	Nimbus	Aurora
Days	86.27%	88.88%	98.69%	100%	66.66%	98.69%
Hours	81.26%	89.1%	97.76%	99.7%	59.47%	98.5%

Using meteorological data, days have been divided into four categories (plus a fifth "NA" category not matching any of the requirements, which is hereby excluded). The "Breeze" regime has been defined as alternating wind directions (WD) between 270 and 70 degrees north (°N) and wind speeds (WS) in the 2–6 m/s interval. The "Eastern Synoptic" regime is defined with a constant WD of 70° and WS $\geq$ 6 m/s. The "Western Synoptic" has the same WS threshold as its eastern counterpart, but the WD is 270°. The "Not Complete" (NC) breeze regime is applied to days with a growing breeze regime, which was later overcome by a regime leaning toward Western synoptic characteristics. In this case, the WS threshold is within 4–8 m/s. All reported WDs have an applicability range of ±15°. Table 3 shows how days whose wind regime falls in one of the above-mentioned categories are distributed over the observation period.

Table 3. Number of days, per month, falling into each of the four wind regime categories.

Months	East. Synoptic	West. Synoptic	Breeze	NC Breeze
May	4	15	1	0
June	1	2	5	0
July	2	4	8	8
August	1	5	8	2
September	0	7	17	0

Analyses have been performed in R 4.4.0 using ggplot2, ggpubr, tidyverse, openair [134,135], zoo, and dplyr packages/libraries to generate hourly/daily aggregations of gathered data. Parameter variability throughout the observation period and daily cycles have been plotted following the methodologies used in previous research on multi-year trends at LMT [111,113,114,117,120]. Ceilometer data have been processed using MATLAB 2016a to generate 2D backscattered profiles [102]. Scatter plots and related correlation data between PBLH and other parameters have also been computed in MATLAB.

3. Results

3.1. Daily Variability During the Observation Period

The campaign evaluated in this study accounts for five months of data gathering at LMT, from 1 May to 30 September 2024. As described in Section 2.1, the Lamezia Terme regional WMO/GAW station is affected by cyclic wind patterns. Figure 2 shows a wind rose based on hourly-aggregated wind speeds and directions.

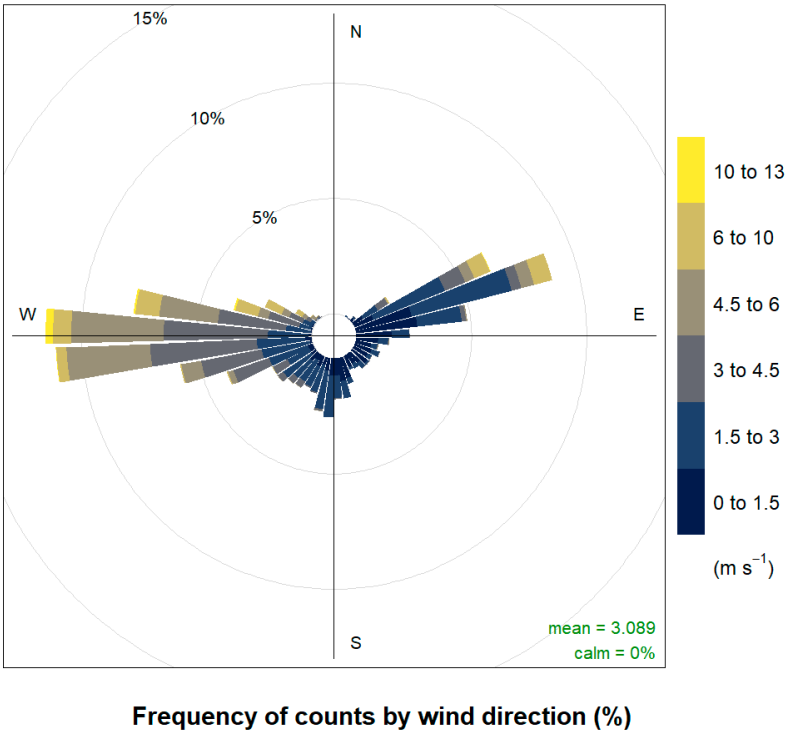

Figure 2. Wind rose based on hourly data gathered during the observation period (1 May–30 September 2024). Calm refers to the reported instances (0%) of a wind speed of 0 m/s.

Data on CO, CO_2, CH_4, eBC, and PM have been gathered on a daily basis to highlight possible trends during the campaign. As reported in Table 2, the coverage rates of these findings vary depending on instrument maintenance and quality assurance. Figure 3 shows hourly aggregated data of all five parameters, with PM data being further divided into multiple subcategories.

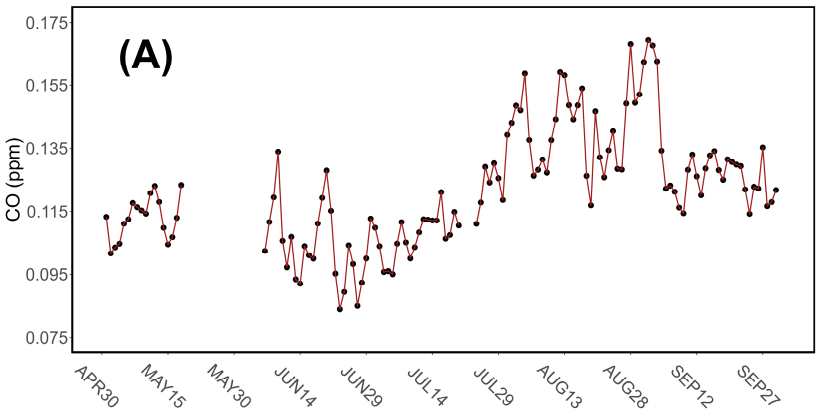

Figure 3. *Cont.*

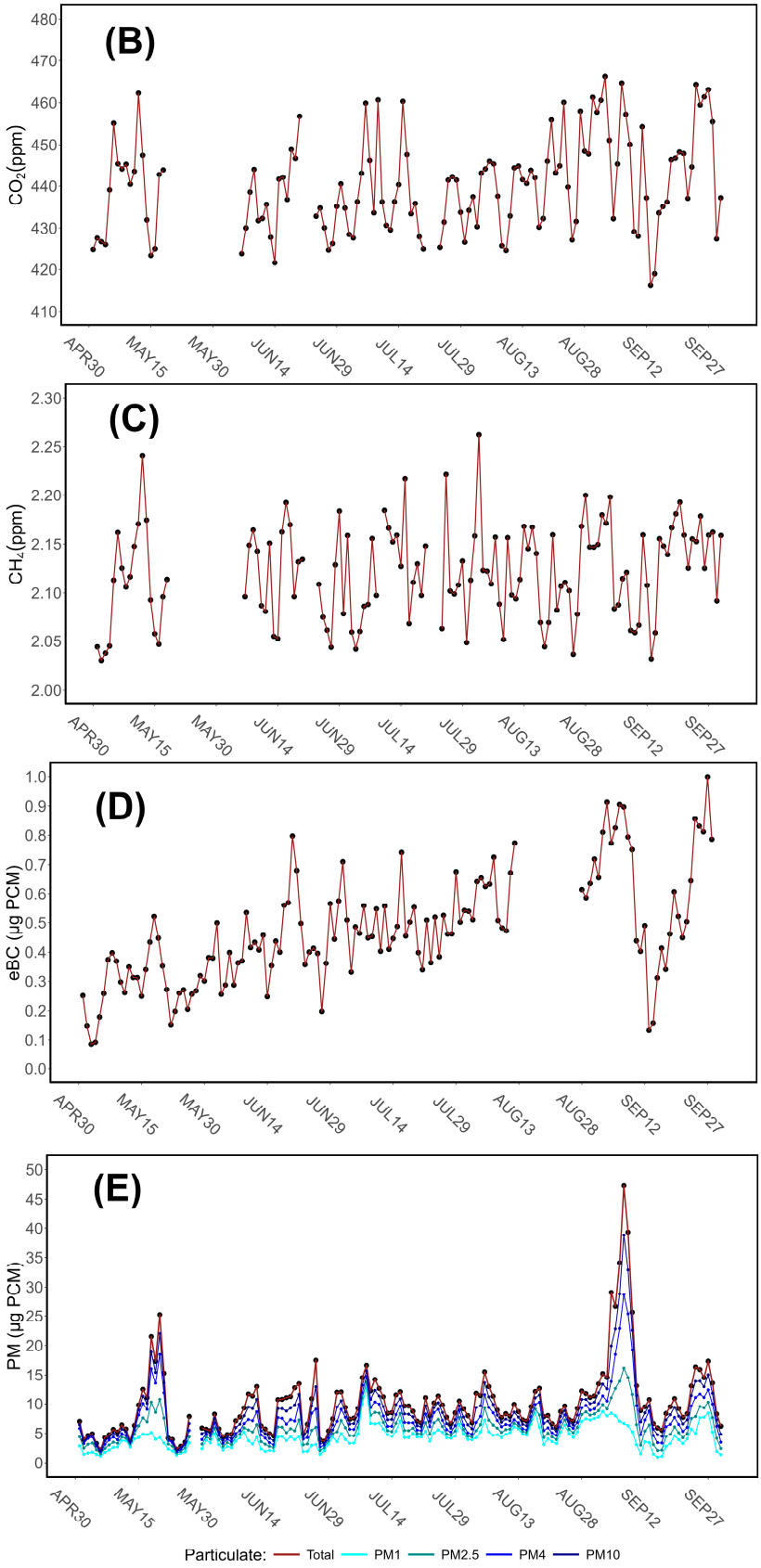

Figure 3. Daily averages of GHG and aerosol parameters evaluated in this research study: (**A**) carbon monoxide (CO), in ppm (parts per million); (**B**) carbon dioxide (CO_2), in ppm; (**C**) methane (CH_4), in

ppm; (**D**) equivalent black carbon (eBC), in µg/m^3; and (**E**) particulate matter (PM) in µg/m^3, divided into the size ranges PM_1, $PM_{2.5}$, PM_4, and PM_{10}. The gaps in CO, CO_2, and CH_4 data shown in A-B-C are due to maintenance issues that affected the Picarro G2401. Similarly, Thermo Scientific 5012 MAAP data gathering was also affected by maintenance, as shown by a gap.

The same analysis has been applied to meteorological and environmental data. Figure 4 shows the daily averages of primary data gathered at LMT during the campaign.

In addition to daily averages, hourly aggregations have also been computed to show variations between May and September 2024 with enhanced details. Figures 5 and 6 show these aggregates for GHG/aerosol and environmental parameters, respectively. Y-axes scales have been adjusted to account for observed peaks.

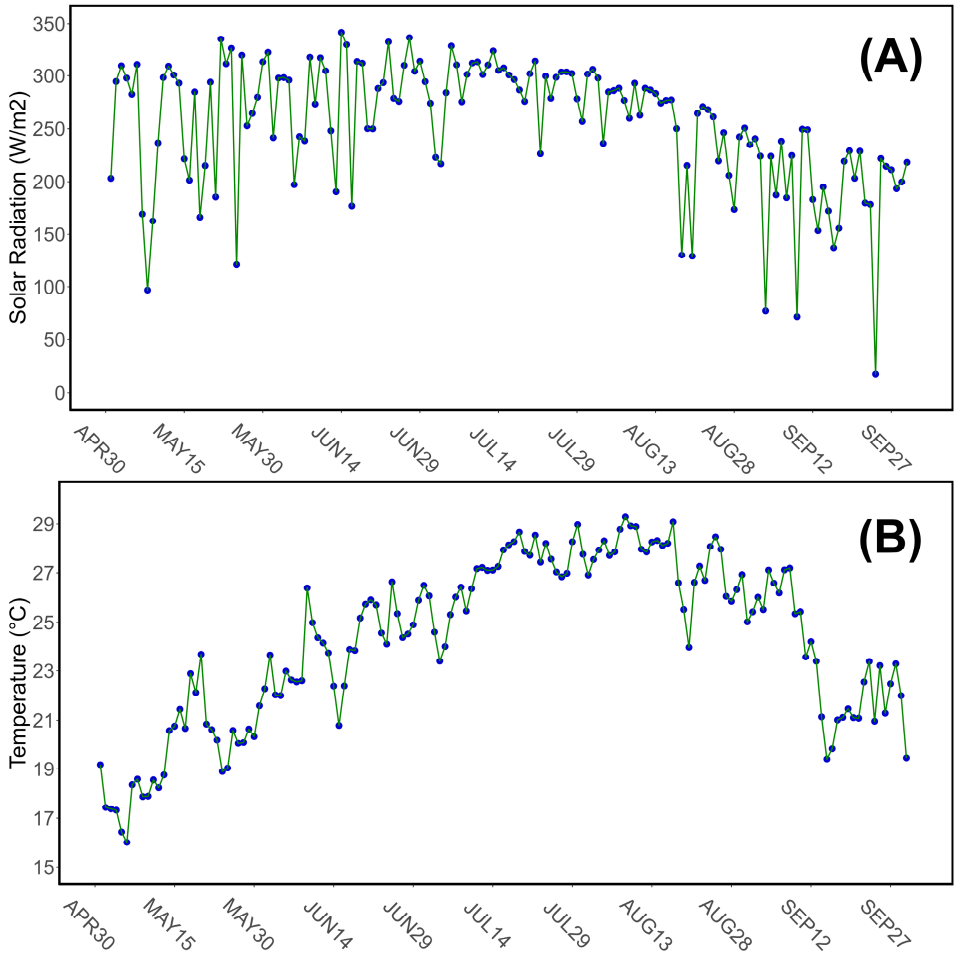

Figure 4. *Cont.*

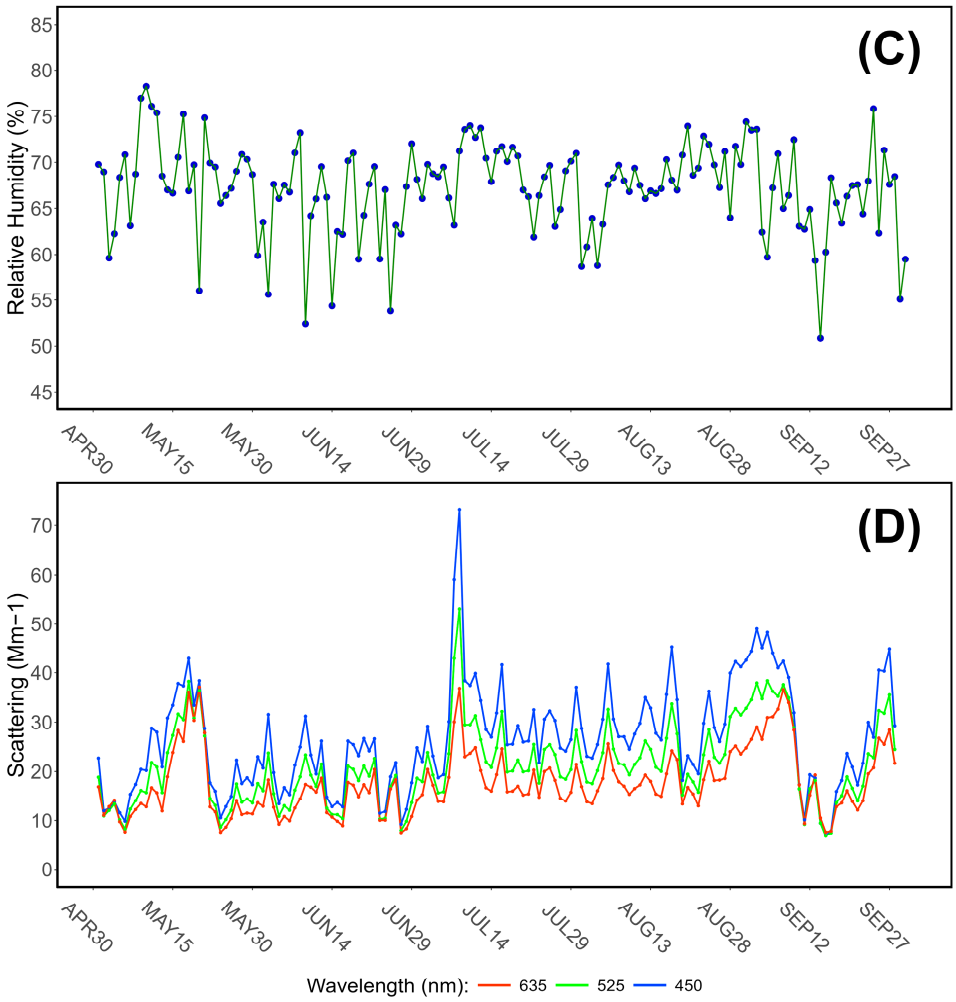

Figure 4. Daily averages of environmental and meteorological data: (**A**) solar radiation in W/m^2; (**B**) temperature in Celsius degrees, °C; (**C**) relative humidity, as a percentage (%); (**D**) scattering, as Mm^{-1}.

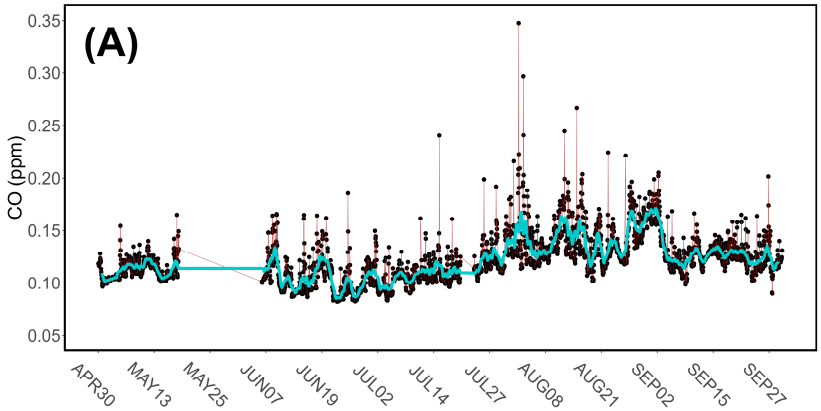

Figure 5. *Cont.*

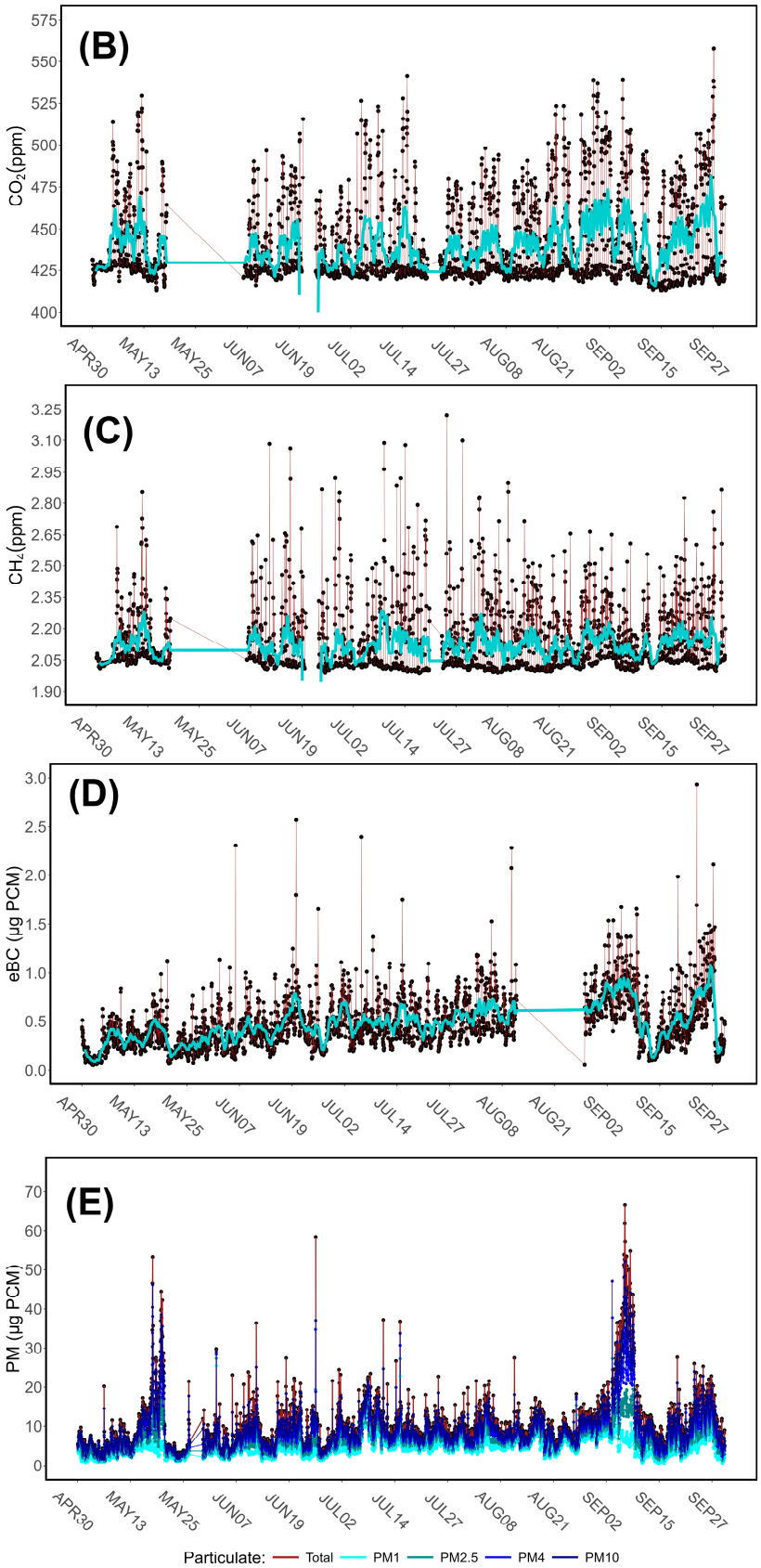

Figure 5. Hourly averages of GHG and aerosol parameters evaluated in this research study: (**A**) carbon monoxide (CO), in ppm (parts per million); (**B**) carbon dioxide (CO_2), in ppm; (**C**) methane (CH_4), in

ppm; (**D**) equivalent black carbon (eBC), in μg/m^3; and (**E**) particulate matter (PM) in μg/m^3, divided into the size ranges PM_1, $PM_{2.5}$, PM_4, and PM_{10}. 36 h moving averages of CO, CO_2, CH_4 (pm), and eBC (μg/m^3) are shown in cyan.

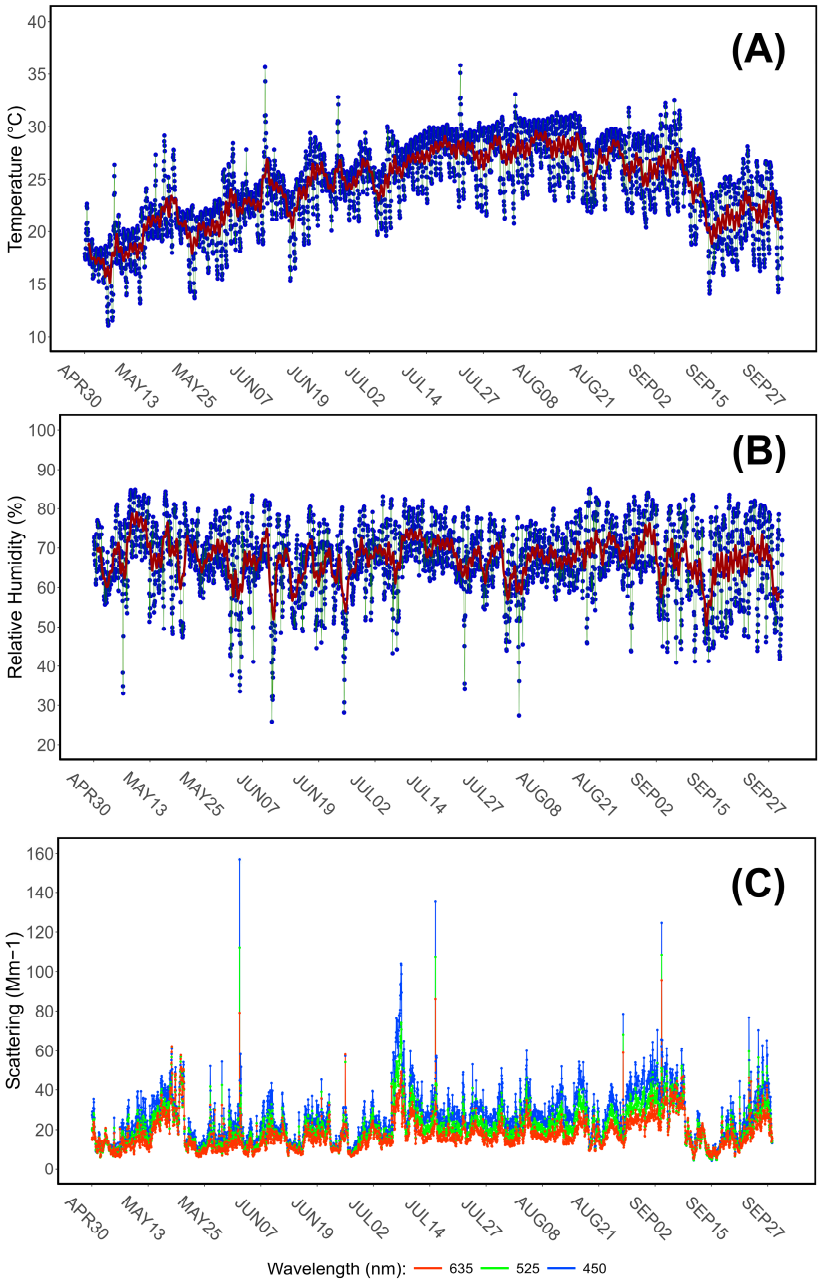

Figure 6. Hourly averages of environmental and meteorological data: (**A**) temperature, in Celsius degrees, °C; (**B**) relative humidity, as a percentage (%); and (**C**) scattering, as Mm^{-1}. 36 h moving averages of T (°C) and RH (%) are shown in dark red.

3.2. Daily Cycles

Research studies on LMT data highlighted the existence of daily cycles [111–114], which are affected by local wind circulation patterns. Up until the campaign presented in this research, these cycles were not assessed under distinct wind regime categories. Figure 7, therefore, shows an enhanced evaluation of the LMT daily cycle of GHGs and aerosol accounting for the four categories described in Section 2.2. Figure 8 shows the daily cycle of key environmental and meteorological parameters.

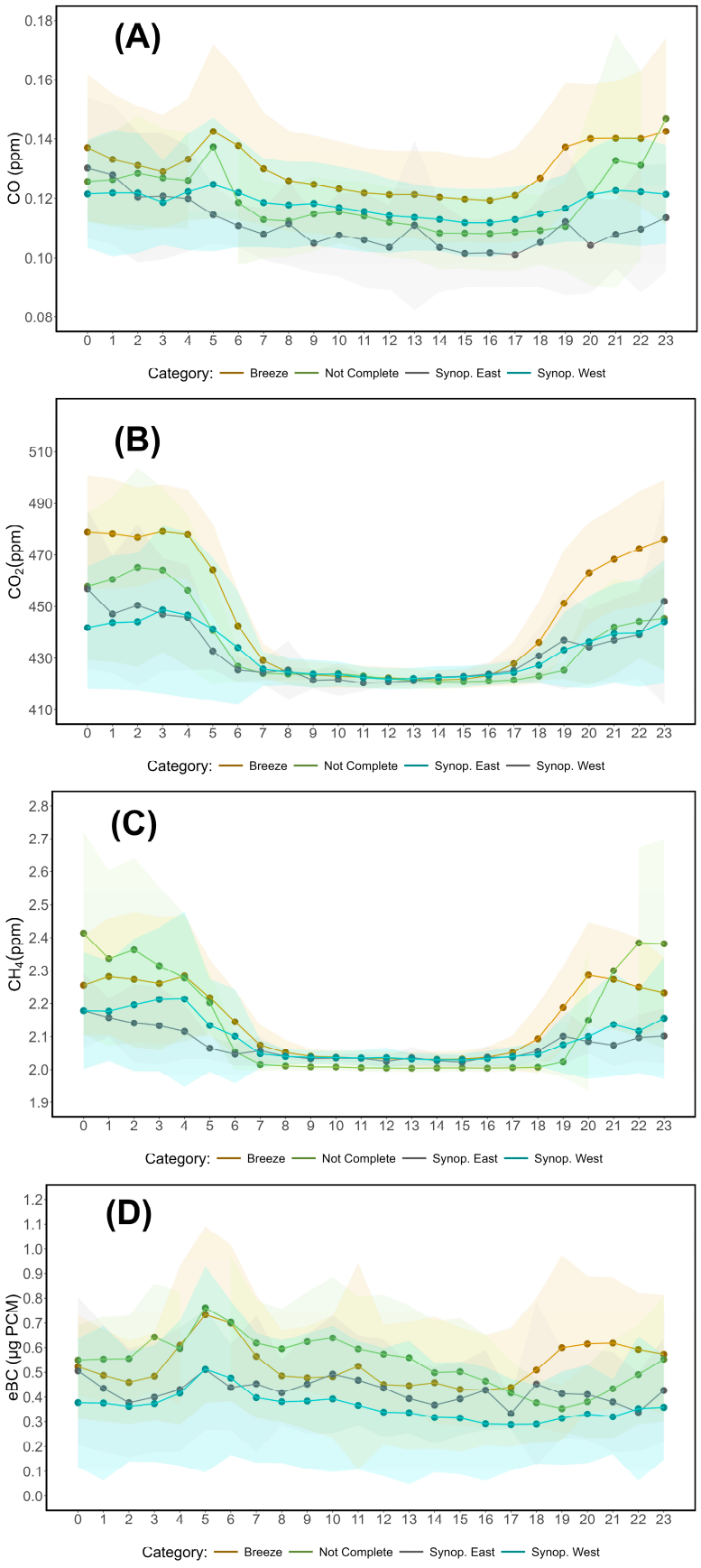

Figure 7. *Cont.*

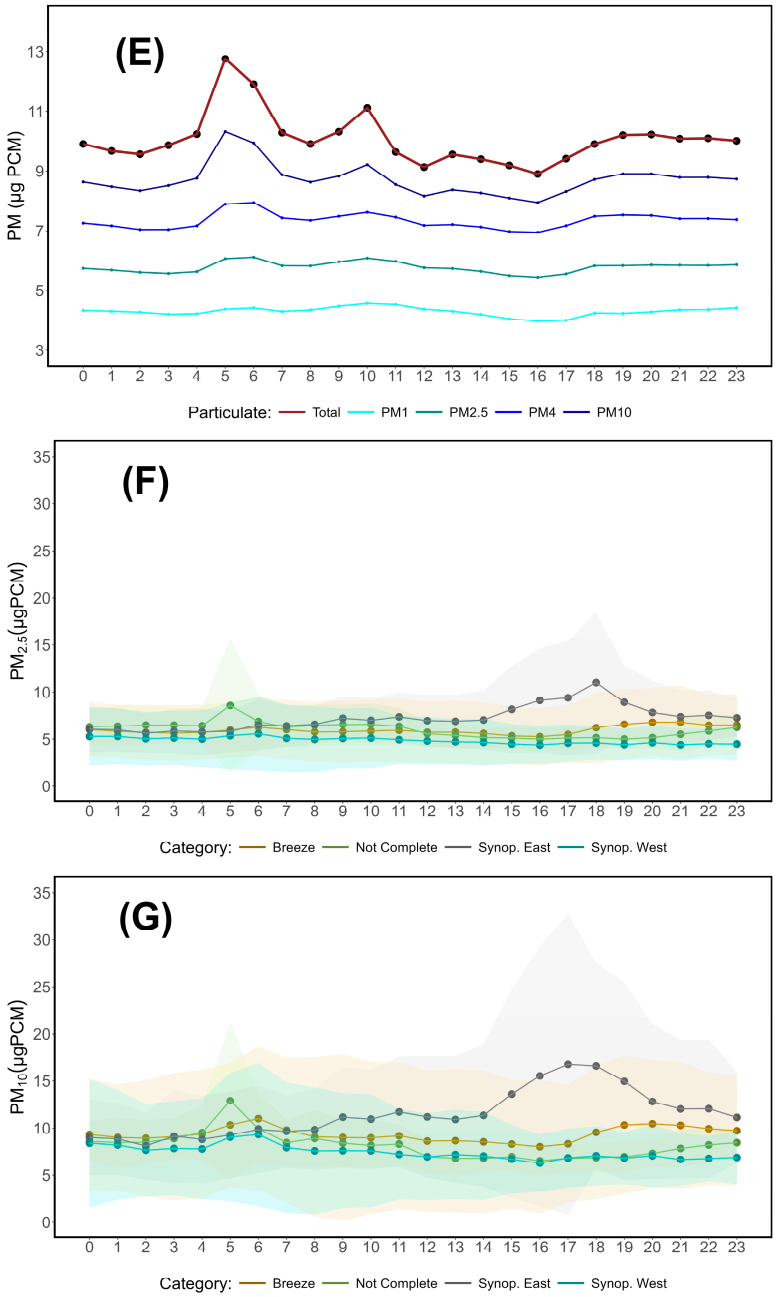

Figure 7. Daily cycles of GHG and aerosol parameters analyzed in this research study, divided by wind regime: (**A**) carbon monoxide (CO), in ppm (parts per million); (**B**) carbon dioxide (CO_2), in ppm; (**C**) methane (CH_4), in ppm; (**D**) equivalent black carbon (eBC), in µg/m^3; (**E**) particulate matter (PM) in µg/m^3, divided into the size ranges PM_1, $PM_{2.5}$, PM_4, and PM_{10} but not accounting for wind regime categories; (**F**) $PM_{2.5}$, with wind regimes; and (**G**) PM_{10}, with wind regimes. Where present, shaded areas refer to intervals within one standard deviation ($\pm\sigma$) from the reported values.

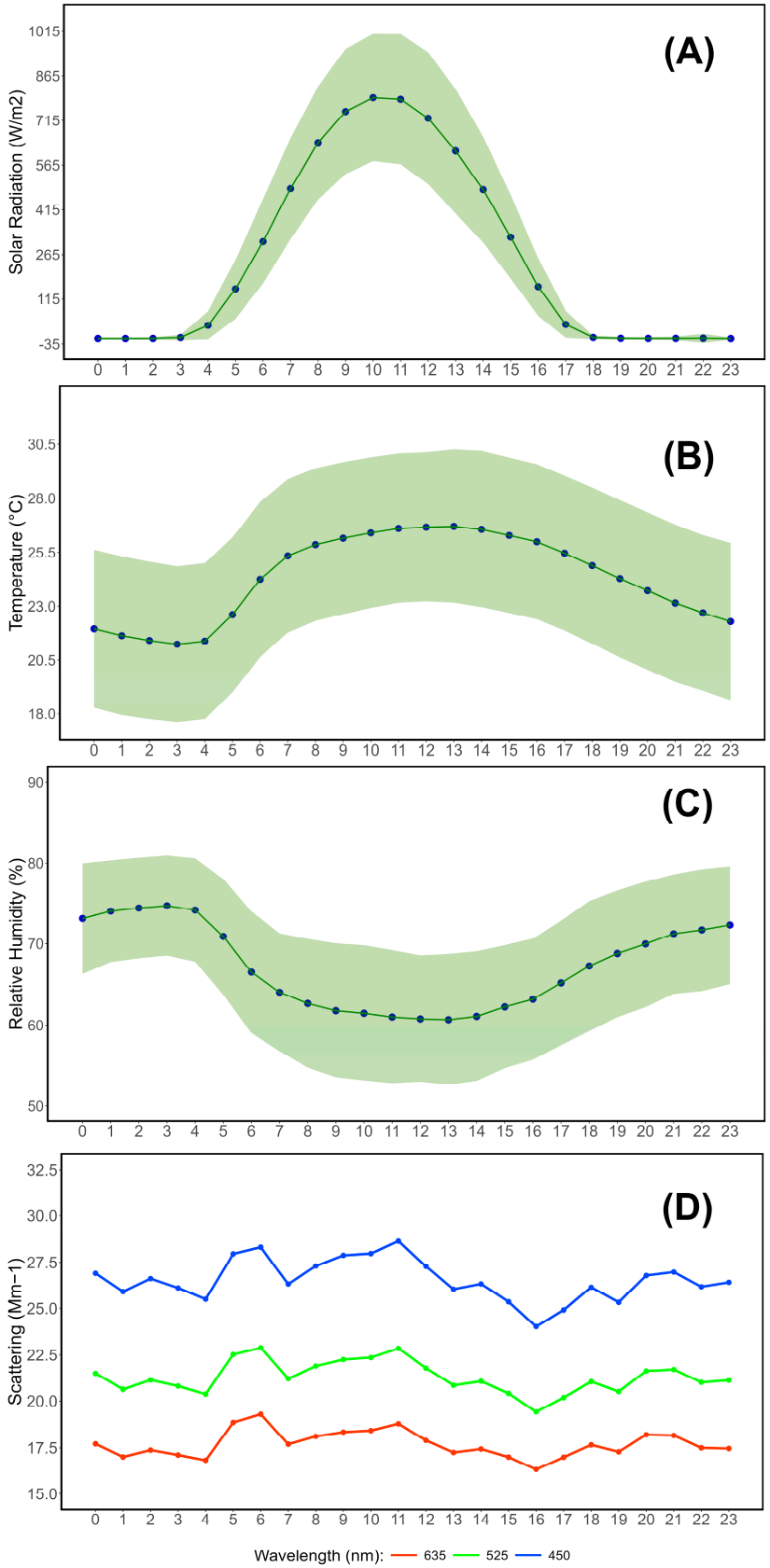

Figure 8. Daily cycles of environmental and meteorological data: (**A**) solar radiation in W/m^2; (**B**) temperature (°C); (**C**) relative humidity (%); and (**D**) scattering (Mm^{-1}). Where present, shaded areas refer to intervals within one standard deviation ($\pm\sigma$) from the reported values.

3.3. Percentile Roses

In D'Amico et al. (2024d) [114], percentile roses have been used to correlate surface ozone concentrations at LMT with specific wind directions. The same method has been used in this research for CO, CO_2, CH_4, eBC, and PM, with the results being reported in Figure 9. $PM_{2.5}$ and PM_{10} have been plotted separately.

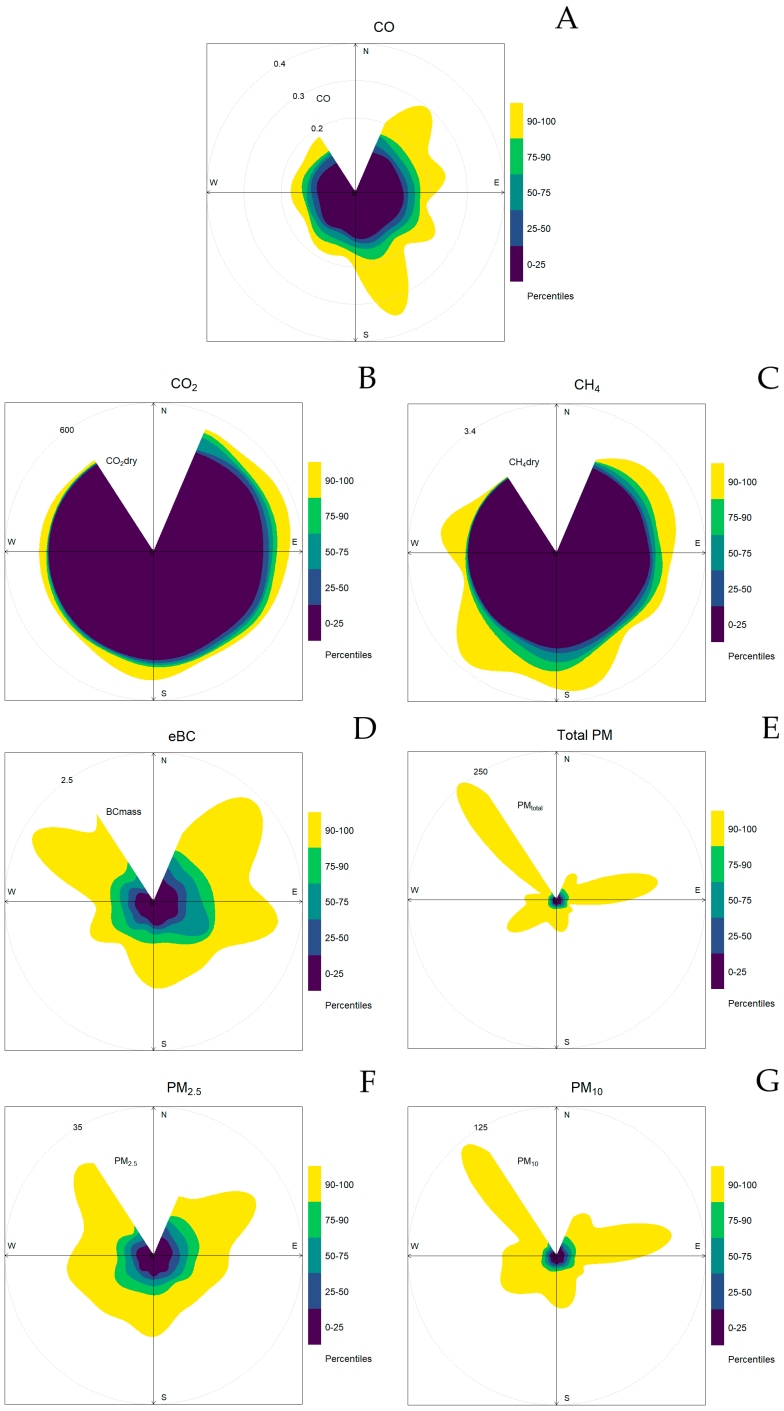

Figure 9. Percentile roses of GHGs and aerosols evaluated in this study. The radius of each rose shows concentrations, while the shaded areas represent the coverage rate by percentile range: (**A**) carbon monoxide (CO), (**B**) carbon dioxide (CO_2), (**C**) methane (CH_4), (**D**) equivalent black carbon (eBC), (**E**) total particulate matter (PM), (**F**) $PM_{2.5}$, and (**G**) PM_{10}.

3.4. Peplospheric Variability and Cycles

Following the evaluation seen in the previous sections with respect to GHGs, aerosols, meteorological, and environmental parameters, the PBLH at Lamezia Terme has been also characterized using daily and hourly averages. The results are shown in Figure 10.

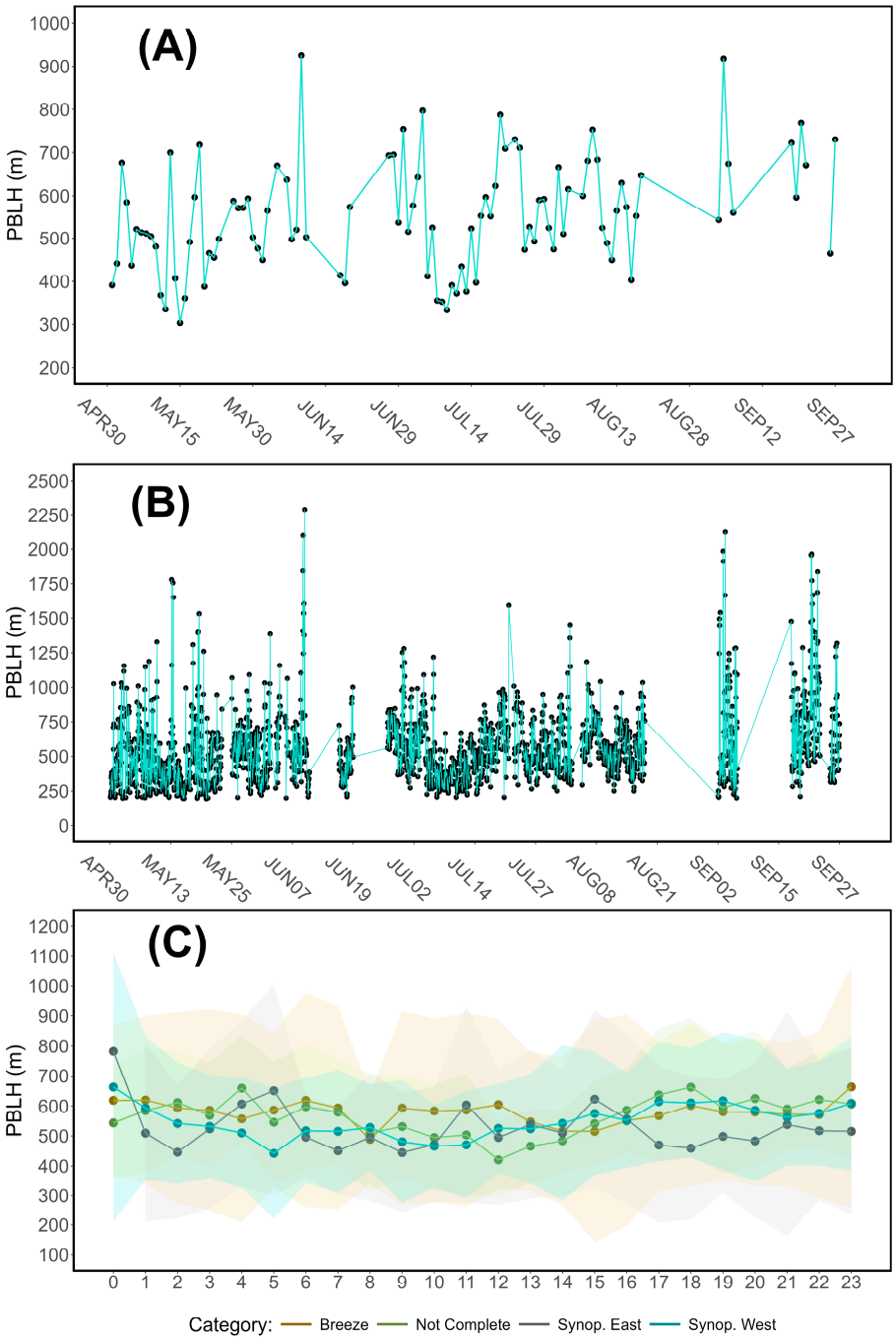

Figure 10. Daily (**A**) and hourly (**B**) averages of PBLH at LMT. Daily cycle (**C**) divided by the four wind regime categories described in Section 2.2. Where present, shaded areas refer to intervals within one standard deviation ($\pm\sigma$) from the reported values.

Vertical profiles of select days deemed representative of all wind regimes have also been plotted using filtered and processed Nimbus data. The results are shown in Figure 11.

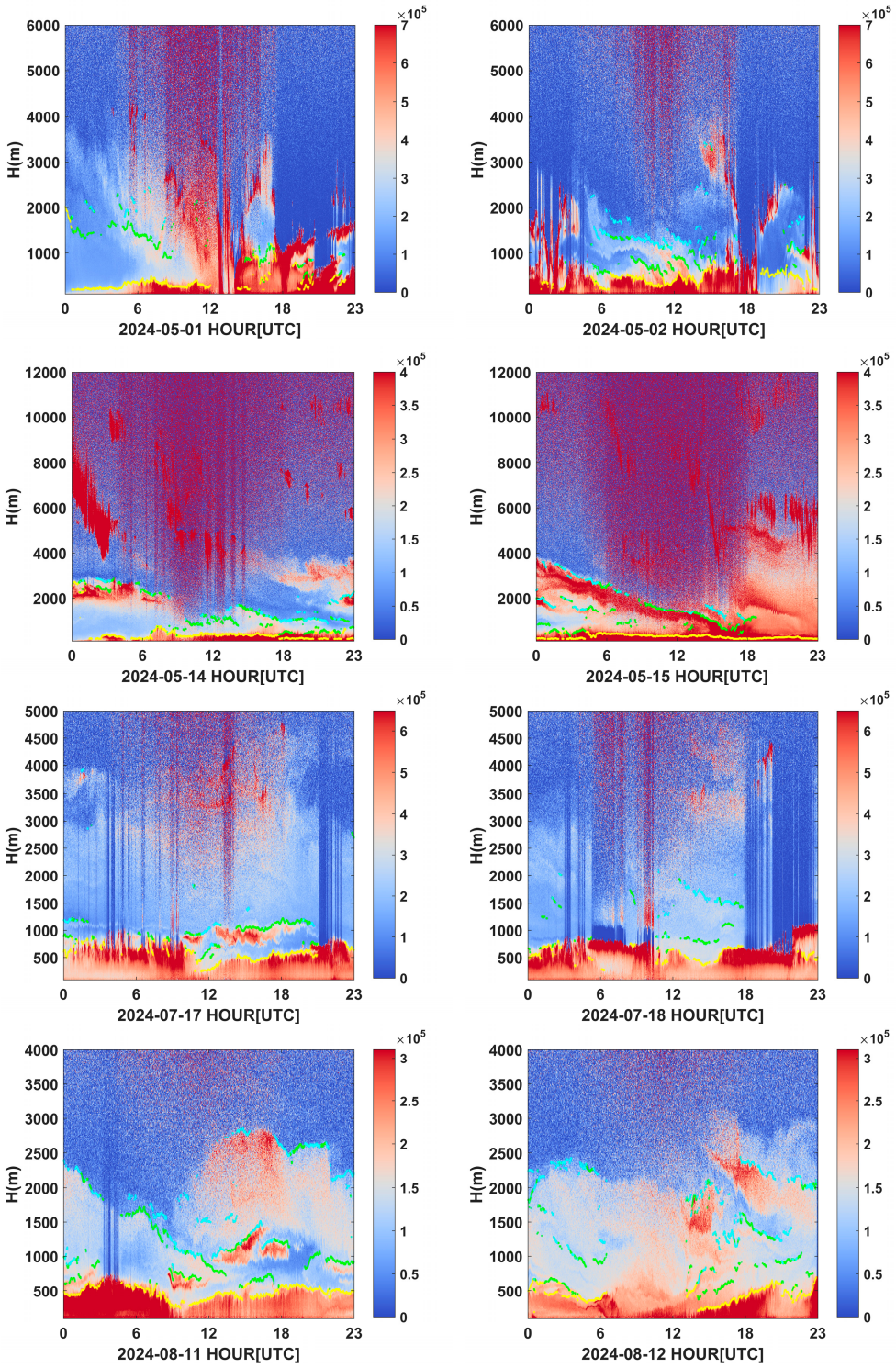

Figure 11. Temporal variation in ceilometer backscattered profiles, aggregated on a 5 min basis, during select days with synoptic flows from west (1, 2 May) and east (14, 15 May), well-developed breeze (11, 12 August), and not complete breeze (17, 18 July). Yellow contours underline PBL boundaries, while turquoise and green contours indicate cloudy layers.

3.5. Correlations Between PBLH, Gases, and Aerosols

Scatter plots of observed parameters (*x*-axis) have been correlated with PBLH (*y*-axis) in Figures 12–17. These plots also show correlation data and the respective *p*-values. For each parameter, the top plots show breeze and not complete breeze regimes, while the bottom ones show western and eastern synoptic flow data, respectively.

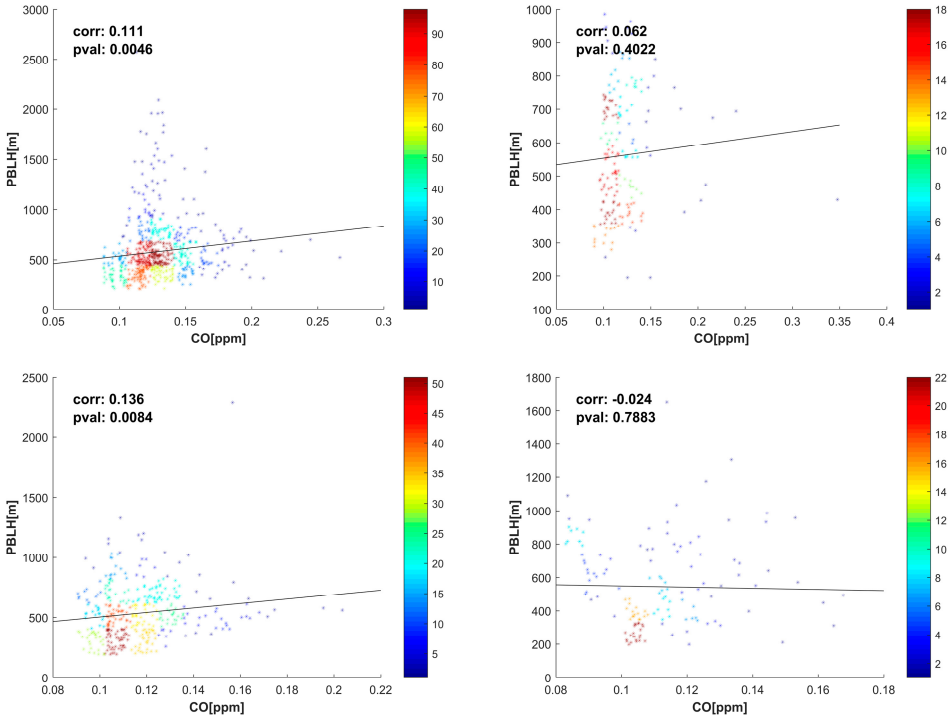

Figure 12. Scatter plots testing the correlation between PBLH and carbon monoxide (CO) under the four observed wind regimes (top: breeze and not complete breeze; bottom: western and eastern synoptic flows).

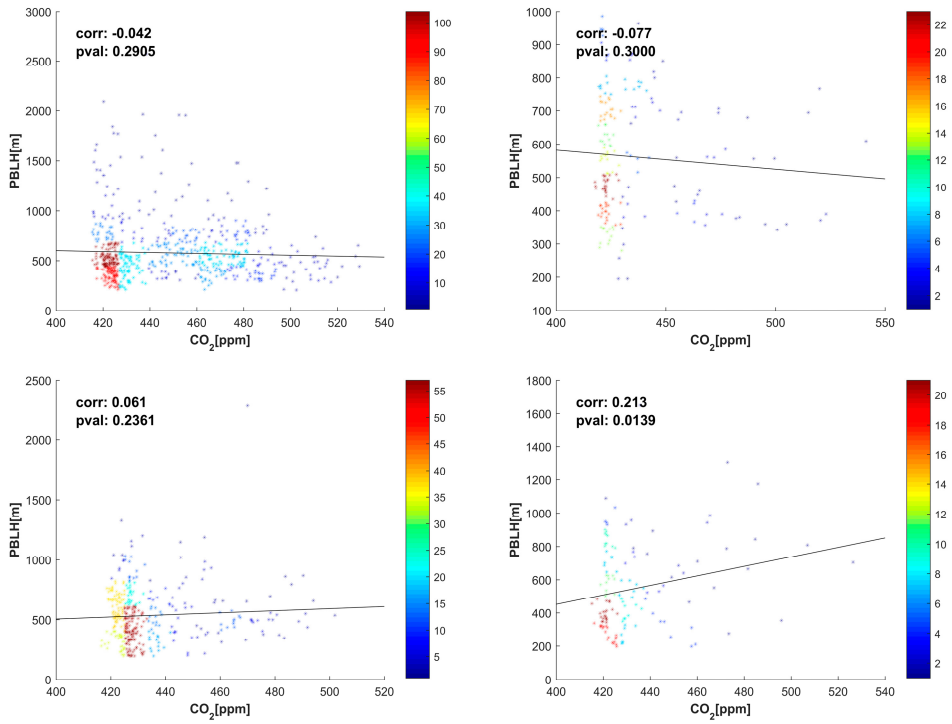

Figure 13. Scatter plots testing the correlation between PBLH and carbon dioxide (CO_2) under the four observed wind regimes (top: breeze and not complete breeze; bottom: western and eastern synoptic flows).

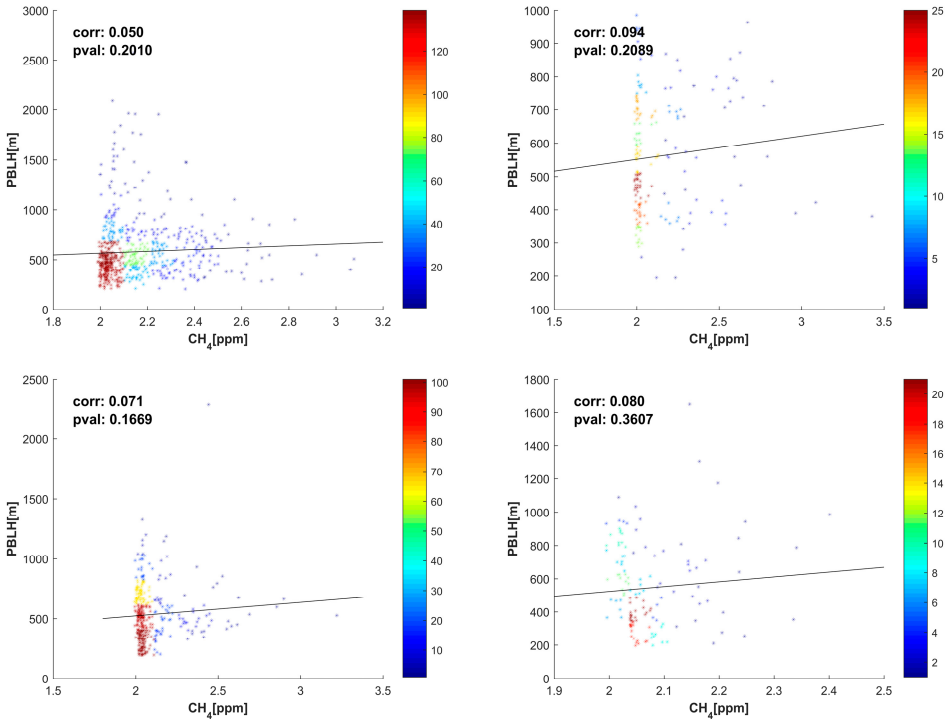

Figure 14. Scatter plots testing the correlation between PBLH and methane (CH_4) under the four observed wind regimes (top: breeze and not complete breeze; bottom: western and eastern synoptic flows).

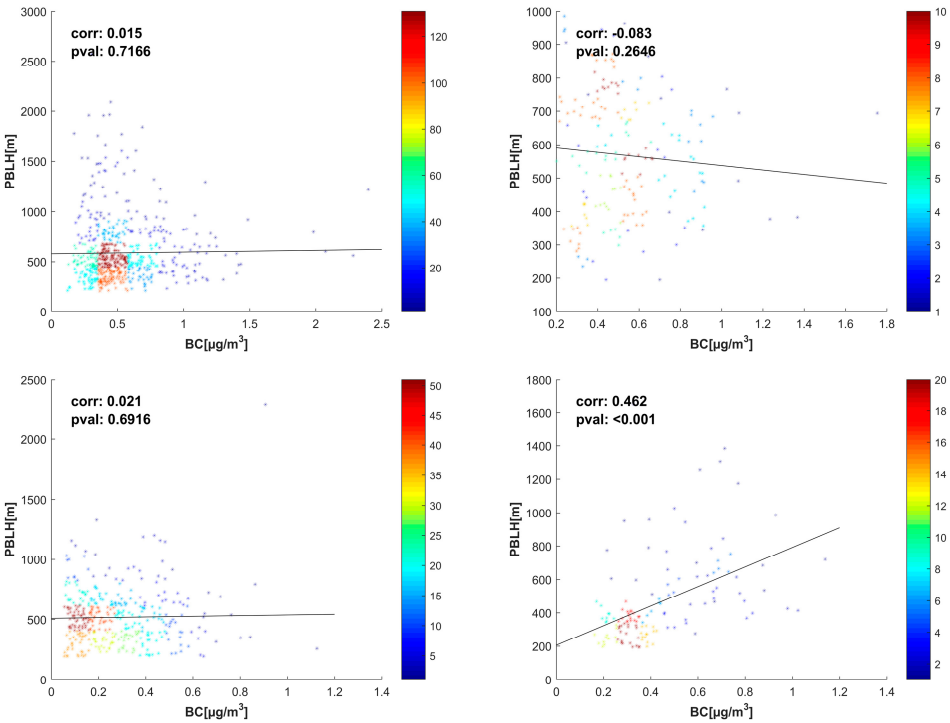

Figure 15. Scatter plots testing the correlation between PBLH and equivalent black carbon (eBC) under the four observed wind regimes (top: breeze and not complete breeze; bottom: western and eastern synoptic flows).

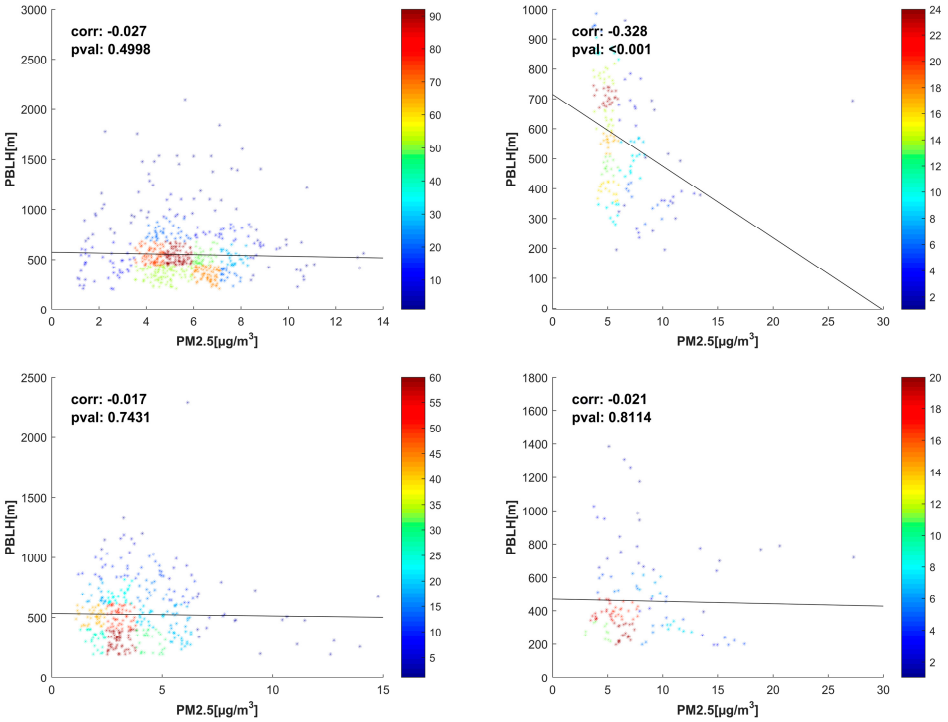

Figure 16. Scatter plots testing the correlation between PBLH and $PM_{2.5}$ under the four observed wind regimes (top: breeze and not complete breeze; bottom: western and eastern synoptic flows).

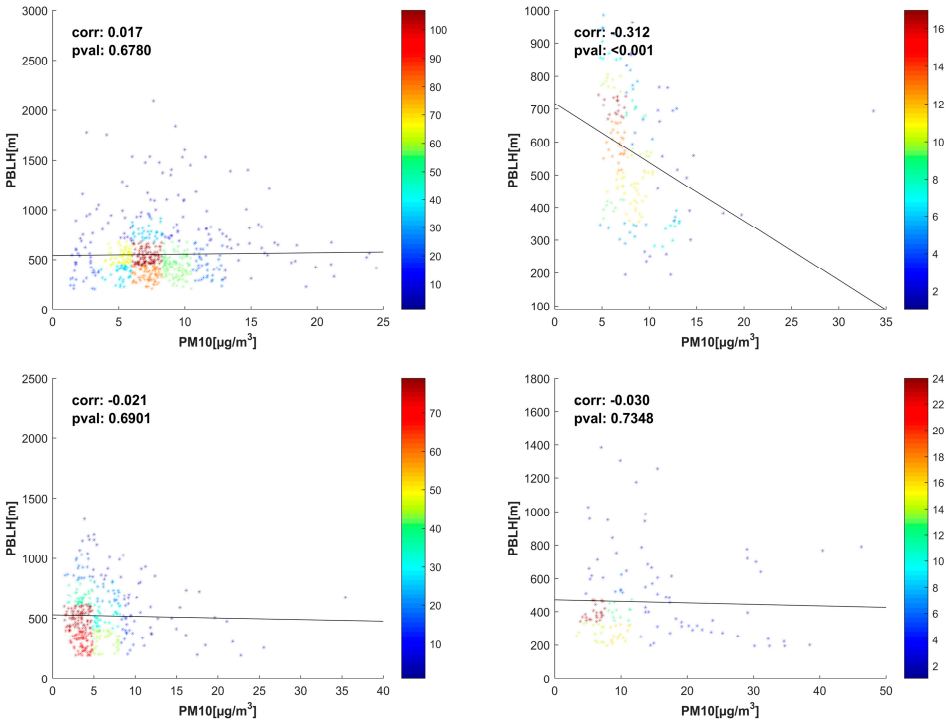

Figure 17. Scatter plots testing the correlation between PBLH and PM_{10} under the four observed wind regimes (top: breeze and not complete breeze; bottom: western and eastern synoptic flows).

The correlation parameters seen in Figures 12–17 have been reported in Table 4. In addition to these data, the correlations between PBLH and key meteorological parameters (relative humidity, RH; temperature, T; downward irradiance, SW) under all wind regimes have also been added to Table 4.

Table 4. Correlation factors and *p*-values of GHGs, aerosol, and meteorological parameters with PBLH (m) under the four wind regime categories. SW correlations are restricted to diurnal hours (10:00–18:00 UTC).

Regime	CO		CH_4		CO_2		eBC		PM_{10}		$PM_{2.5}$		RH		T		SW	
	corr	*p*val	corr	*p*val	corr	*p*val	corr	*p*val	corr	*p*val	corr	*p*val	corr	*p*val	corr	*p*val	corr	*p*val
Breeze	0.11	0.004	0.05	0.21	0.04	0.29	0.015	0.716	0.017	0.67	−0.027	0.5	−0.188	<0.001	−0.058	0.119	−0.02	0.76
NC Breeze	0.062	0.402	0.092	0.209	−0.077	0.3	0.083	0.26	−0.312	<0.001	−0.328	<0.001	−0.081	0.263	0.040	0.581	−0.360	<0.001
Syn. East	−0.024	0.78	0.08	0.36	0.213	0.014	0.462	<0.001	−0.03	0.734	−0.021	0.811	0.097	0.195	0.138	0.065	−0.367	<0.001
Syn. West	0.136	0.0083	0.071	0.167	0.061	0.236	0.021	0.691	−0.021	0.69	−0.017	0.743	−0.161	<0.001	0.146	<0.001	−0.0013	0.127

4. Discussion

A campaign focused on peplosphere or planetary boundary layer (PBL) characterization has been performed at the Lamezia Terme regional WMO/GAW observation site in Calabria, Southern Italy. The campaign relied on a new ceilometer (Table 1), a longer observation span compared to previous comparable research, and the integration of additional data (specifically, GHGs and aerosols, see Table 2) meant to test correlations that were not applicable during the summer 2009 campaign described in Lo Feudo et al. (2020) [102]. Specifically, the previous campaign was limited to 23 days (15 July–6 August 2009), and the employed ceilometer was a different model (Vaisala CL31—Vantaa, Finland). The CL31 transmitted laser pulses on a vertical axis and measured backscattered signals, which were correlated with the scattering particles present in the column. With a data gathering frequency of one acquisition per second, the CL31 operated at a wavelength of 910 nm, with a maximum operating range of 7500 m and a resolution of 20 m [136]. The previous campaign lacked the measurement of CO, CO_2, CH_4, eBC, and PM concentrations necessary to expand on the correlation between peplospheric variability and other parameters.

The preliminary evaluation of environmental data allowed us to define the fundamentals upon which the findings of this campaign would be based. Local wind circulation patterns are oriented on a W/NE axis [107,108], as shown in Figure 2. GHG and aerosol data coverage, in addition to meteorological parameters, show both daily (Figures 3 and 4) and hourly (Figures 5 and 6) variability during the observation period.

Following the analyses seen in other research papers focused on LMT data [111,113,114,117], daily cycles of GHGs, aerosols, and meteorological parameters have been assessed. LMT has been proven in multiple studies to have a peculiar daily cycle, and this research effectively integrates a new variable, peplosphere height variability, into these cycles. In the case of GHGs and aerosols, the analysis has considered four distinct wind regimes, each defined by specific direction (WD) and speed (WS) thresholds: breeze, not complete (NC) breeze, eastern synoptic, and western synoptic (Table 3). In the case of CO_2 (Figure 7B) and CH_4 (Figure 7C), although the breeze and NC breeze yield higher values during night-time hours, diurnal concentrations are lower and do not show differences in terms of wind regime. However, CO (Figure 7A), eBC (Figure 7D), and PM (Figure 7E–G) show greater variability in morning and evening hours that is compatible with inversions in wind patterns from the northeastern-continental to the western-seaside corridors, and vice versa. PM (Figure 7F,G) is particularly susceptible to night-time fluctuations. The susceptibility of pollutant concentrations to inversions in wind patterns was first reported in Cristofanelli et al. (2017) [111] and further supported in D'Amico et al. (2024c) [117], which analyzed the first 2020 COVID-19 lockdown in Italy to highlight the nature of pollutant peaks linked to wind circulation in lockdown versus ante/post lockdown periods.

Key meteorological and environmental parameters show well-defined daily cycles (Figure 8). In particular, scattering values (Figure 8D) show a peak linked to increased pollutant surface concentrations that occur during inversions.

The percentile roses in Figure 9 differentiate between gases and aerosols in terms of spatial distribution. Two types of behavior are reported: minor spatial variations, as seen in the case of CO_2 (Figure 9B) and CH_4 (Figure 9C); intermediate variations, as in the case of CO (Figure 9A), eBC (Figure 9D), and $PM_{2.5}$ (Figure 9F); substantial variations, seen

specifically in PM_{10} (Figure 9G). These differences reflect not only the susceptibility of each parameter to wind regimes but also indicate distinct emission sources. CO and eBC, which are both effective tracers of combustion processes, were linked to local wildfires in a previous research study by Malacaria et al. (2024) [122]. CH_4 is characterized by both natural and anthropogenic sources, and local peaks are linked to northeastern-continental winds [113]. In Cristofanelli et al. (2017) [111], methane peaks at LMT were specifically attributed to sources located nearby via the combined implementation of atmospheric tracers.

Particulate matter, based on its size, are indicator of distinct emission sources. In fact, as described in Section 1, PM is heterogeneous in nature. Anthropogenic $PM_{2.5}$ emissions are generally linked, for example, to fossil fuel burning and domestic heating, while PM_{10} is linked to natural sources such as sea spray, biomass burning attributable to agriculture, Saharan dust events [121], and wildfires [122]. Among the anthropogenic sources of PM_{10}, incomplete fossil fuel-burning processes are common. The findings of this research study allow to narrow down the nature of observed PM depending on the four wind regimes that affect LMT observations: The breeze is linked to diurnal sea spray from the west and nocturnal smog from the northeast; the not complete (NC) breeze results into a southern corridor and PM peaks that are hereby interpreted as biomass burning linked to agricultural activities; the western synoptic regime combines sea spray outputs with continental-anthropogenic PM; the eastern synoptic regime is linked to all PM categories.

In Figure 10, PBLH data have been plotted to show the overall variability during the observation period, as well as the daily cycle (Figure 10C). This cycle in particular shows daily PBLH variations depending on the four distinct categories of wind regimes, which in turn have an impact on gas and aerosol concentrations observed at LMT. Examples of the four categories are shown in Figure 11.

Scatter plots testing the correlation of PBLH, gases, and aerosols have been plotted in Figures 12–17 under all four wind regimes. An apparent inverse relationship or anticorrelation between PBLH and CO_2 and CH_4 concentrations can be seen in Figures 13 and 14. This suggests that as the PBLH increases, CO_2 and CH_4 concentrations tend to decrease, indicating that lower peplosphere heights correspond to limited vertical mixing and the accumulation of these gases near the surface. The results of the correlations tested in Figures 12–17, as well as additional tests accounting for RH, T, and SW (irradiance evaluations were restricted to diurnal hours, between 10:00 and 18:00 UTC), have been reported in Table 4. With respect to meteorological parameters, the correlations are positive with the exception of temperature under the breeze regime, due to the sea/land breeze phenomenon. The correlation between relative humidity and PBLH is negative under all wind regimes, with the exception of eastern synoptic conditions. In the case of SW, there are minor negative correlations due to the fact that diurnal solar irradiance alone has been considered, and solar irradiance in May and September is lower compared to their summer peak counterparts. In the case of gases and aerosols, all correlations are positive with the exception of CO under eastern synoptic conditions. CO_2's correlation with PBLH is generally positive, except for the NC breeze regime. eBC is particularly sensitive to PBLH variability, as it shows the highest correlation factor among all parameters in the case of eastern synoptic wind regimes. PM_{10} is positively correlated with the breeze regime, and the correlation with other regimes has a minor negative tendency. In $PM_{2.5}$'s case, there are minor negative correlations with PBLH under all wind regimes.

In the analysis of this study's results, it is worth mentioning the contribution of the ash sphere, which can be natural or anthropogenic in origin [137,138], on a number of parameters addressed in this study. As ash particles absorb sunlight, a local increase in temperature can occur: This form of heating would then perturb atmospheric circulation and the consequent transport of GHGs and aerosols; fluctuations in temperature and solar radiation can also alter chemical processes in the atmosphere, further contributing to the perturbation of the system [139].

Overall, when synoptic conditions are favorable to sea breeze development, colder air masses from the sea with low marine aerosol content are advected over land in the early morning and interact with the nighttime boundary layer. After the onset of the sea breeze, an internal boundary layer develops from the coastal discontinuity and the height of the maximum backscatter threshold from the Nimbus decreases, likely due to the advection of the marine aerosols above the peplosphere, thus creating a discontinuity in aerosol concentration and size distribution. Later in the morning, when the breeze is well developed, the convection takes over and mixes marine and continental aerosols, creating a homogeneous content of aerosols filling the convective layer.

During stationary synoptic flow with wind speed typically > 5 m/s, marine aerosols are mixed with their continental counterparts and the height of the boundary layer detected by LMT's ceilometer remains constant. During sea breeze days, at the onset of the breeze, the findings of this research and past studies indicate that the sea breeze advection of marine aerosols causes a nonhomogeneous columnar distribution, inducing a low LiDAR signal-to-noise ratio above the internal boundary layer [102].

Figures 12–17 show that the advection of cleaner air with marine aerosols from the sea with respect to the land aerosols, flowing above the internal boundary layer, after the breeze onset, causes a vertical discontinuity of aerosol concentration and thus a reduction in the LiDAR vertical range. In the case of breeze, the resulting values of PBLH vary as expected following the daily cycle over land, i.e., low during the stable night and high during the unstable days. During synoptic flow, the peplosphere is constantly higher compared to unstable conditions. It is therefore reported that during the night, synoptic PBLH is higher than during the day. A reason can be that during summer the breeze always develops, adding and modulating the synoptic flow (Figure 11). A well-developed breeze, adding speed, would produce a large quantity of marine aerosols advected on land flowing over the land; the aerosol layer would contribute to the detection of a lower PBLH.

Seasonality is likely to play a role in the observed correlation between wind regimes, PBLH, and the atmospheric concentrations of gases and aerosols. Future works are set to cover a longer period of time and cover the winter season, which was not covered in the two campaigns (2009 and 2024) due to no instrument availability. At LMT, many of the observed parameters are known from previous research to be affected by seasonal cycles [111,113,114,117,120], so the introduction of PBLH as an additional variable will contribute to an enhanced characterization of LMT.

Compared to the previous campaign from 2009, in this research, it is observed that PBLH is characterized by high degrees of variability during eastern and western synoptic conditions. The mixed layer causing pollutants to reach higher altitudes matches the findings of the previous campaign.

Therefore, the findings of this research provide evidence of direct peplospheric influences over the surface concentrations of GHGs and aerosols. With respect to urban air quality management, these findings may be used by policymakers and regulators to pinpoint circumstances of reduced air quality under specific pollution/peplospheric conditions and counteract accordingly (e.g., via selective bans of vehicular traffic). The applicability of the same methodologies employed in this study for the assessment of peplospheric influences on other stations across the globe could be possible; however, Lamezia Terme (LMT) shows, at least in the context of the Italian monitoring network, a unique geographic configuration in the narrowest point of the entire peninsula, the Catanzaro isthmus, with a local wind circulation that is channeled through the isthmus itself and results into characteristic daily cycles and wind regimes. In addition to the peculiarity of LMT's location in the Tyrrhenian coast of Calabria, the Mediterranean basin has shown differences in trends and chemical/atmospheric processes affecting compounds such as methane [140] and ozone [141,142] between its western and eastern sectors; considering that LMT is located at the center of the Mediterranean and its observations are likely influenced by this variability, atmospheric monitoring stations in other parts of the globe could yield different results.

5. Conclusions

This research work relied on an enhanced characterization of peplospheric variability at the Lamezia Terme (code: LMT) regional coastal WMO/GAW observation site in Calabria, Southern Italy. The study is based on five continuous months (May–September 2024) of PBLH data obtained by a Nimbus ceilometer, plus GHG, aerosol, meteorological, and environmental data gathered by other instruments. The integration of multiple datasets has ensured a more detailed understanding of peplospheric variability at the site, as the previous campaign on PBLH was focused entirely on one month of observations performed during the 2009 summer season, and no correlations with the surface concentrations of key pollutants were possible at the time.

This study has introduced four distinct categories of wind regimes (breeze, not complete breeze, eastern synoptic, western synoptic) and tested the correlation of PBLH variability with the concentrations of carbon monoxide (CO), carbon dioxide (CO_2), methane (CH_4), equivalent black carbon (eBC), and particulate matter (PM) under each regime. Due to the heterogeneous value of these parameters, different correlations have been tested: eBC has yielded the highest correlation value among all parameters under the eastern synoptic regime, a corridor that previous research studies on LMT data have correlated with higher anthropogenic outputs.

Overall, these findings demonstrate the need to effectively integrate PBLH data and wind regimes in urban air quality assessments due to the influence of PBLH patterns on the surface concentration of key pollutants. Such a study demonstrates the importance of correlating circulation, complex orography, and boundary conditions at the interface between land and sea when dealing with the assessment of natural and anthropogenic pollutants. The availability of physical/chemical and aerosol data allows us to test the correlation between PBLH variability and a number of factors.

The new findings further expand on the data obtained during the 2009 campaign and corroborate the hypotheses from the previous study on mixed-layer behavior at the site.

The LMT observation site is therefore a challenging natural laboratory for capturing different circulation patterns in which natural and anthropic-induced pollutant concentrations show different behaviors. Future research integrating the findings shown in this study with additional parameters will further demonstrate the importance of considering all these factors in sustainable policies/regulations and air quality monitoring.

Author Contributions: Conceptualization, F.D. and T.L.F.; methodology, F.D. and T.L.F.; software, F.D., D.G., S.S., G.D.B. and T.L.F.; validation, C.R.C., I.A., D.G., S.S., G.D.B. and T.L.F.; formal analysis, F.D., D.G., G.D.B. and T.L.F.; investigation, F.D., D.G., G.D.B. and T.L.F.; data curation, F.D., I.A., D.G., L.M., S.S., G.D.B. and T.L.F.; writing—original draft preparation, F.D., C.R.C. and T.L.F.; writing—review and editing, F.D., C.R.C., I.A., D.G., L.M., S.S., G.D.B. and T.L.F.; visualization, F.D., C.R.C., D.G., L.M., S.S., G.D.B. and T.L.F.; supervision, C.R.C. and T.L.F.; funding acquisition, C.R.C. All authors have read and agreed to the published version of the manuscript.

Funding: This research was funded by AIR0000032—ITINERIS, the Italian Integrated Environmental Research Infrastructures System (D.D. n. 130/2022—CUP B53C22002150006) under the EU—Next Generation EU PNRR—Mission 4 "Education and Research"—Component 2: "From research to business"—Investment 3.1: "Fund for the realization of an integrated system of research and innovation infrastructures".

Data Availability Statement: The datasets presented in this article are not readily available because they are part of other ongoing studies. ALICEnet data are available through the dedicated online platform.

Acknowledgments: The authors would like to acknowledge the efforts of the five anonymous reviewers who contributed to improving and expanding the manuscript and would also like to thank the editorial staff for their support.

Conflicts of Interest: The authors declare no conflicts of interest.

References

1. Buajitti, K.; Blackadar, A.K. Theoretical studies of diurnal wind-structure variations in the planetary boundary layer. *Bound. Layer Meteorol.* **1957**, *83*, 486–500. [CrossRef]
2. Barry, P.J.; Munn, R.E. Use of radioactive tracers in studying mass transfer in the atmospheric boundary layer. *Phys. Fluids* **1967**, *10*, S263–S266. [CrossRef]
3. Estoque, M.A.; Bhumralkar, C.M. A method for solving the planetary boundary-layer equations. *Bound. Layer Meteorol.* **1970**, *1*, 169–194. [CrossRef]
4. Godev, N. On the cyclogenetic nature of the Earth's orographic form. *Arch. Met. Geoph. Biokl. A* **1970**, *19*, 299–310. [CrossRef]
5. Clarke, R.H. Observational studies in the atmospheric boundary layer. *Q. J. R. Meteorol. Soc.* **1970**, *96*, 91–114. [CrossRef]
6. Telford, J.W. The surface roughness and planetary boundary layer. *Pure Appl. Geophys.* **1980**, *119*, 278–293. [CrossRef]
7. Stewart, R.W.; Wilson, J.R.; Burling, R.W. Some statistical properties of small scale turbulence in an atmospheric boundary layer. *J. Fluid Mech.* **1970**, *41*, 141–152. [CrossRef]
8. Van Atta, C.W.; Chen, W.Y. Structure functions of turbulence in the atmospheric boundary layer over the ocean. *J. Fluid Mech.* **1970**, *44*, 145–159. [CrossRef]
9. Garratt, J.R.; Francey, R.J. Bulk characteristics of heat transfer in the unstable, baroclinic atmospheric boundary layer. *Bound. Layer Meteorol.* **1978**, *15*, 399–421. [CrossRef]
10. Schönwald, B. Determination of vertical temperature profiles for the atmospheric boundary layer by ground-based microwave radiometry. *Bound. Layer Meteorol.* **1978**, *15*, 453–464. [CrossRef]
11. Arya, S.P.S. Comparative effects of stability, baroclinity and the scale-height ratio on drag laws for the atmospheric boundary layer. *J. Atmos. Sci.* **1978**, *35*, 40–46. [CrossRef]
12. Zhao, M. A numerical experiment of the PBL with geostrophic momentum approximation. *Adv. Atmos. Sci.* **1988**, *5*, 47–56. [CrossRef]
13. Angell, J.K. Correlations in the vertical component of the wind at heights of 600, 1600 and 2600 ft at Cardington. *Q. J. R. Meteorol. Soc.* **1964**, *90*, 307–312. [CrossRef]
14. Stull, R.B. *An Introduction to Boundary Layer Meteorology*; Kluwer Academic Publishers: Dordrecht, The Netherlands, 1988; p. 666. [CrossRef]
15. Stensrud, D.J. *Parameterization Schemes: Keys to Understanding Numerical Weather Prediction Models*; Cambridge University Press: Cambrige, UK, 2007; p. 459. [CrossRef]
16. Liu, S.; Liang, X.Z. Observed diurnal cycle climatology of planetary boundary layer height. *J. Clim.* **2010**, *23*, 5790–5809. [CrossRef]
17. Wang, W.; Gong, W.; Mao, F.; Pan, Z. An Improved Iterative Fitting Method to Estimate Nocturnal Residual Layer Height. *Atmosphere* **2016**, *7*, 106. [CrossRef]
18. Bakas, N.A.; Fotiadi, A.; Kariofillidi, S. Climatology of the Boundary Layer Height and of the Wind Field over Greece. *Atmosphere* **2020**, *11*, 910. [CrossRef]
19. Gu, J.; Zhang, Y.H.; Yang, N.; Wang, R. Diurnal variability of the planetary boundary layer height estimated from radiosonde data. *Earth Planet. Phys.* **2020**, *4*, 479–492. [CrossRef]
20. Rao, K.S.; Snodgrass, H.F. Some parameterizations of the nocturnal boundary layer. *Bound. Layer Meteorol.* **1979**, *17*, 15–28. [CrossRef]
21. Mahrt, L.; Heald, R.C.; Lenschow, D.H.; Stankov, B.B.; Troen, I.B. An observational study of the structure of the nocturnal boundary layer. *Bound. Layer Meteorol.* **1979**, *17*, 247–264. [CrossRef]
22. Hsu, S.A. Mesoscale nocturnal jetlike winds within the planetary boundary layer over a flat, open coast. *Bound. Layer Meteorol.* **1979**, *17*, 485–494. [CrossRef]
23. Sawyer, V.; Li, Z. Detection, variation and intercomparison of the planetary boundary layer depth from radiosonde, lidar and infrared spectrometer. *Atmos. Environ.* **2013**, *79*, 518–528. [CrossRef]
24. Coen, M.C.; Praz, C.; Haefele, A.; Ruffieux, D.; Kaufmann, P.; Calpini, B. Determination and climatology of the planetary boundary layer height above the Swiss plateau by in situ and remote sensing measurements as well as by the COSMO-2 model. *Atmos. Chem. Phys.* **2014**, *14*, 13205–13221. [CrossRef]
25. Hanna, S.R. The thickness of the planetary boundary layer. *Atmos. Environ.* **1969**, *3*, 519–536. [CrossRef]
26. Smeda, M.S. A bulk model for the atmospheric planetary boundary layer. *Bound. Layer Meteorol.* **1979**, *17*, 411–427. [CrossRef]
27. Odintsov, S.; Miller, E.; Kamardin, A.; Nevzorova, I.; Troitsky, A.; Schröder, M. Investigation of the Mixing Height in the Planetary Boundary Layer by Using Sodar and Microwave Radiometer Data. *Environments* **2021**, *8*, 115. [CrossRef]
28. Els, N.; Baumann-Stanzer, K.; Larose, C.; Vogel, T.M.; Sattler, B. Beyond the planetary boundary layer: Bacterial and fungal vertical biogeography at Mount Sonnblick, Austria. *Geo Geogr. Environ.* **2019**, *6*, e00069. [CrossRef]
29. Tignat-Perrier, R.; Dommergue, A.; Vogel, T.M.; Larose, C. Microbial Ecology of the Planetary Boundary Layer. *Atmosphere* **2020**, *11*, 1296. [CrossRef]
30. Anthes, R.A. The height of the planetary boundary layer and the production of circulation in a sea breeze model. *J. Atmos. Sci.* **1978**, *35*, 1231–1239. [CrossRef]
31. Kao, S.K.; Yeh, E.N. A model of the effects of stack and inversion heights on the transport and diffusion of pollutants in the planetary boundary layer. *Atmos. Environ.* **1979**, *13*, 873–878. [CrossRef]

32. Dunst, M. Ergebnisse von Modellrechnungen zur Ausbreitung von Stoffbeimengungen in der planetarischen Grenzschicht. *Z. Meteorol.* **1980**, *30*, 47–59.
33. Jordanov, D.L.; Dzolov, G.D.; Sirakov, D.E. Effect of planetary boundary layer on long-range transport and diffusion of pollutants. *C. R. Acad. Bulg. Sci.* **1979**, *32*, 1635–1637.
34. McNider, R.T.; Moran, M.D.; Pielke, R.A. Influence of diurnal and inertial boundary-layer oscillations on long-range dispersion. *Atmos. Environ.* **1988**, *22*, 2445–2462. [CrossRef]
35. Farah, A.; Freney, E.; Chauvigné, A.; Baray, J.-L.; Rose, C.; Picard, D.; Colomb, A.; Hadad, D.; Abboud, M.; Farah, W.; et al. Seasonal Variation of Aerosol Size Distribution Data at the Puy de Dôme Station with Emphasis on the Boundary Layer/Free Troposphere Segregation. *Atmosphere* **2018**, *9*, 244. [CrossRef]
36. Raptis, I.-P.; Kazadzis, S.; Amiridis, V.; Gkikas, A.; Gerasopoulos, E.; Mihalopoulos, N. A Decade of Aerosol Optical Properties Measurements over Athens, Greece. *Atmosphere* **2020**, *11*, 154. [CrossRef]
37. Butler, M.P.; Lauvaux, T.; Feng, S.; Liu, J.; Bowman, K.W.; Davis, K.J. Atmospheric Simulations of Total Column CO_2 Mole Fractions from Global to Mesoscale within the Carbon Monitoring System Flux Inversion Framework. *Atmosphere* **2020**, *11*, 787. [CrossRef]
38. Lee, P.; Ngan, F. Coupling of Important Physical Processes in the Planetary Boundary Layer between Meteorological and Chemistry Models for Regional to Continental Scale Air Quality Forecasting: An Overview. *Atmosphere* **2011**, *2*, 464–483. [CrossRef]
39. Zhao, D.; Tie, X.; Gao, Y.; Zhang, Q.; Tian, H.; Bi, K.; Jin, Y.; Chen, P. In-Situ Aircraft Measurements of the Vertical Distribution of Black Carbon in the Lower Troposphere of Beijing, China, in the Spring and Summer Time. *Atmosphere* **2015**, *6*, 713–731. [CrossRef]
40. Zhou, Q.; Cheng, L.; Zhang, Y.; Wang, Z.; Yang, S. Relationships between Springtime $PM_{2.5}$, PM_{10}, and O_3 Pollution and the Boundary Layer Structure in Beijing, China. *Sustainability* **2022**, *14*, 9041. [CrossRef]
41. Zhang, X.; Li, Z.; Ming, J.; Wang, F. One-Year Measurements of Equivalent Black Carbon, Optical Properties, and Sources in the Urumqi River Valley, Tien Shan, China. *Atmosphere* **2020**, *11*, 478. [CrossRef]
42. Abbass, K.; Qasim, M.Z.; Song, H.; Murshed, M.; Mahmood, H.; Younis, I. A review of the global climate change impacts, adaptation, and sustainable mitigation measures. *Environ. Sci. Pollut. Res.* **2022**, *29*, 42539–42559. [CrossRef]
43. Endlich, R.M.; Ludwig, F.L.; Uthe, E.E. An automatic method for determining the mixing depth from lidar observations. *Atmos. Environ.* **1979**, *13*, 1051–1056. [CrossRef]
44. Sicard, M.; Pérez, C.; Comerón, A.; Baldasano, J.M.; Rocadenbosch, F. Determination of the mixing layer height from regular lidar measurements in the Barcelona Area. *Proc. SPIE Int. Soc. Opt. Eng.* **2004**, *5235*, 505–516. [CrossRef]
45. Münkel, C.; Räsänen, J. New optical concept for commercial lidar ceilometers scanning the boundary layer. *Proc. SPIE Int. Soc. Opt. Eng.* **2004**, *5571*, 364–374. [CrossRef]
46. Emeis, S.; Schäfer, K. Remote Sensing Methods to Investigate Boundary-layer Structures relevant to Air Pollution in Cities. *Bound. Layer Meteorol.* **2006**, *121*, 377–385. [CrossRef]
47. Emeis, S.; Schäfer, K.; Münkel, C. Surface-based remote sensing of the mixing-layer height: A review. *Meteorol. Z.* **2008**, *17*, 621–630. [CrossRef]
48. Melfi, S.H.; Spinhirne, J.D.; Chou, S.-H.; Palm, S.P. Lidar observations of vertically organized convection in the planetary boundary layer over the ocean. *J. Clim. Appl. Meteorol.* **1985**, *24*, 806–821. [CrossRef]
49. Pierson, W.J. Importance of the atmospheric boundary layer over the oceans in synoptic scale meteorology. *Phys. Fluids* **1967**, *10*, S203–S205. [CrossRef]
50. Raynor, G.S.; Sethuraman, S.; Brown, R.M. Formation and characteristics of coastal internal boundary layers during onshore flows. *Bound. Layer Meteorol.* **1979**, *16*, 487–514. [CrossRef]
51. Burk, S.D.; Haack, T.; Samelson, R.M. Mesoscale simulation of supercritical, subcritical, and transcritical flow along coastal topography. *J. Atmos. Sci.* **1999**, *56*, 2780–2795. [CrossRef]
52. Edwards, K.A.; Rogerson, A.M.; Winant, C.D.; Rogers, D.P. Adjustment of the marine atmospheric boundary layer to a coastal cape. *J. Atmos. Sci.* **2001**, *58*, 1511–1528. [CrossRef]
53. Helmis, C.G. An experimental case study of the mean and turbulent characteristics of the vertical structure of the atmospheric boundary layer over the sea. *Meteorol. Z.* **2007**, *16*, 375–381. [CrossRef]
54. Mastrantonio, G.; Petenko, I.; Viola, A.; Argentini, S.; Coniglio, L.; Monti, P.; Leuzzi, G. Influence of the synoptic circulation on the local wind field in a coastal area of the Tyrrhenian Sea. *Earth Environ. Sci.* **2008**, *1*, 1–9. [CrossRef]
55. Peña, A.; Gryning, S.-E.; Hahmann, A.N. Observations of the atmospheric boundary layer height under marine upstream flow conditions at a coastal site. *J. Geophys. Res. Atmos.* **2013**, *118*, 1924–1940. [CrossRef]
56. Caicedo, V.; Rappenglueck, B.; Cuchiara, G.; Flynn, J.; Ferrare, R.; Scarino, A.J.; Berkoff, T.; Senff, C.; Langford, A.; Lefer, B. Bay breeze and sea breeze circulation impacts on the planetary boundary layer and air quality from an observed and modeled DISCOVER-AQ Texas case study. *J. Geophys. Res. Atmos.* **2019**, *124*, 7359–7378. [CrossRef]
57. Barantiev, D.; Batchvarova, E.; Novitsky, M. Breeze circulation classification in the coastal zone of the town of Ahtopol based on data from ground based acoustic sounding and ultrasonic anemometer. *Bulg. J. Meteorol. Hydrol.* **2017**, *22*, 2–25.
58. Lyulyukin, V.; Kallistratova, M.; Zaitseva, D.; Kuznetsov, D.; Artamonov, A.; Repina, I.; Petenko, I.V.; Kouznetsov, R.; Pashkin, A. Sodar Observation of the ABL Structure and Waves over the Black Sea Offshore Site. *Atmosphere* **2019**, *10*, 811. [CrossRef]

59. Dang, R.; Yang, Y.; Hu, X.-M.; Wang, Z.; Zhang, S. A Review of Techniques for Diagnosing the Atmospheric Boundary Layer Height (ABLH) Using Aerosol Lidar Data. *Remote. Sens.* **2019**, *11*, 1590. [CrossRef]
60. Wilson, D. Quantifying and comparing fuel-cycle greenhouse-gas emissions: Coal, oil and natural gas consumption. *Energy Policy* **1990**, *18*, 550–562. [CrossRef]
61. Scheraga, J.D.; Leary, N.A. Improving the efficiency of policies to reduce CO_2 emissions. *Energy Policy* **1992**, *20*, 394–404. [CrossRef]
62. Smith, I.M. CO_2 and climatic change: An overview of the science. *Energy Convers. Manag.* **1993**, *34*, 729–735. [CrossRef]
63. Zhao, F.; Zeng, N. Continued increase in atmospheric CO_2 seasonal amplitude in the 21st century projected by the CMIP5 Earth system models. *Earth Syst. Dynam.* **2014**, *5*, 423–439. [CrossRef]
64. Keeling, C.D.; Whorf, T.P.; Wahlen, M.; van der Plichtt, J. Interannual extremes in the rate of rise of atmospheric carbon dioxide since 1980. *Nature* **1995**, *375*, 666–670. [CrossRef]
65. Mabbutt, J.A. Impacts of carbon dioxide warming on climate and man in the semi-arid tropics. *Clim. Change* **1989**, *15*, 191–221. [CrossRef]
66. Jain, P.C. Greenhouse effect and climate change: Scientific basis and overview. *Renew. Energy* **1993**, *3*, 403–420. [CrossRef]
67. Allen, J.G.; MacNaughton, P.; Satish, U.; Santanam, S.; Vallarino, J.; Spengler, J.D. Associations of cognitive function scores with carbon dioxide, ventilation, and volatile organic compound exposures in office workers: A controlled exposure study of green and conventional office environments. *Environ. Health Perspect.* **2016**, *124*, 805–812. [CrossRef]
68. Smith, M.R.; Golden, C.D.; Myers, S.S. Potential rise in iron deficiency due to future anthropogenic carbon dioxide emissions. *GeoHealth* **2017**, *1*, 248–257. [CrossRef] [PubMed]
69. Perera, F.; Ashrafi, A.; Kinney, P.; Mills, D. Towards a fuller assessment of benefits to children's health of reducing air pollution and mitigating climate change due to fossil fuel combustion. *Environ. Res.* **2019**, *172*, 55–72. [CrossRef]
70. Bolin, B.; Eriksson, E. Changes in the carbon dioxide content of the atmosphere and sea due to fossil fuel combustion. In *The Atmosphere and The Sea in Motion Scientific Contributions to the Rossby Memorial Volume*; Bolin, B., Ed.; The Rockefeller Institute Press: New York, NY, USA, 1959; pp. 130–142.
71. Edwards, D.P.; Emmons, L.K.; Hauglustaine, D.A.; Chu, D.A.; Gille, J.C.; Kaufman, Y.J.; Pétron, G.; Yurganov, L.N.; Giglio, L.; Deeter, M.N.; et al. Observations of carbon monoxide and aerosols from the Terra satellite: Northern Hemisphere variability. *J. Geophys. Res. Atmos.* **2004**, *109*, 17. [CrossRef]
72. Zheng, B.; Chevallier, F.; Ciais, P.; Yin, Y.; Deeter, M.N.; Worden, H.M.; Wang, Y.; Zhang, Q.; He, K. Rapid decline in carbon monoxide emissions and export from East Asia between years 2005 and 2016. *Environ. Res. Lett.* **2018**, *13*, 044007. [CrossRef]
73. Khalil, M.A.K.; Rasmussen, R.A. Carbon Monoxide in the Earth's Atmosphere: Increasing Trend. *Science* **1984**, *223*, 54–56. [CrossRef]
74. Buchholz, R.R.; Worden, H.M.; Park, M.; Francis, G.; Deeter, M.N.; Edwards, D.P.; Emmons, L.K.; Gaubert, B.; Gille, J.; Martínez-Alonso, S.; et al. Air pollution trends measured from Terra: CO and AOD over industrial, fire-prone, and background regions. *Remote Sens. Environ.* **2021**, *256*, 112275. [CrossRef]
75. Prather, M.J. Lifetimes and time scales in atmospheric chemistry. *Philos. Trans. R. Soc. A* **2007**, *365*, 1705–1726. [CrossRef] [PubMed]
76. Marenco, A. Variations of CO and O_3 in the troposphere: Evidence of O_3 photochemistry. *Atmos. Environ.* **1986**, *20*, 911–918. [CrossRef]
77. Szopa, S.; Naik, V.; Adhikary, B.; Artaxo, P.; Berntsen, T.; Collins, W.D.; Fuzzi, S.; Gallardo, L.; Kiendler-Scharr, A.; Klimont, Z.; et al. Short-Lived Climate Forcers. In *Climate Change 2021: The Physical Science Basis. Contribution of Working Group I to the Sixth Assessment Report of the Intergovernmental Panel on Climate Change*; Masson-Delmotte, V., Zhai, P., Pirani, A., Connors, S.L., Péan, C., Berger, S., Caud, N., Chen, Y., Goldfarb, L., Gomis, M.I., et al., Eds.; Cambridge University Press: Cambridge, UK, 2021; pp. 817–922.
78. Skeie, R.B.; Hodnebrog, Ø.; Myhre, G. Trends in atmospheric methane concentrations since 1990 were driven and modified by anthropogenic emissions. *Commun. Earth Environ.* **2023**, *4*, 317. [CrossRef]
79. Saunois, M.; Stavert, A.R.; Poulter, B.; Bousquet, P.; Canadell, J.G.; Jackson, R.B.; Raymond, P.A.; Dlugokencky, E.J.; Houweling, S.; Patra, P.K.; et al. The Global Methane Budget 2000–2017. *Earth Syst. Sci. Data* **2020**, *12*, 1561–1623. [CrossRef]
80. Lee, D.S.; Fahey, D.; Forster, P.M.; Newton, P.J.; Wit, R.C.N.; Lim, L.L.; Owen, B.; Sausen, R. Aviation and global climate change in the 21st century. *Atmos. Environ.* **2009**, *43*, 3520–3537. [CrossRef]
81. Lee, D.S.; Fahey, D.W.; Skowron, A.; Allen, M.R.; Burkhardt, U.; Chen, Q.; Doherty, S.J.; Freeman, S.; Forster, P.M.; Fuglestvedt, J.; et al. The contribution of global aviation to anthropogenic climate forcing for 2000 to 2018. *Atmos. Environ.* **2021**, *244*, 117834. [CrossRef]
82. Nisbet, E.G.; Fisher, R.E.; Lowry, D.; France, J.L.; Allen, G.; Bakkaloglu, S.; Broderick, T.J.; Cain, M.; Coleman, M.; Fernandez, J.; et al. Methane Mitigation: Methods to Reduce Emissions, on the Path to the Paris Agreement. *Rev. Geophys.* **2020**, *58*, e2019RG000675. [CrossRef]
83. Horvath, H. Atmospheric light absorption: A review. *Atmos. Environ. Part A* **1993**, *27*, 293–317. [CrossRef]
84. Chameides, W.L.; Bergin, M. Soot takes center stage. *Science* **2002**, *297*, 2214–2215. [CrossRef]

85. Bond, T.C.; Doherty, S.J.; Fahey, D.W.; Forster, P.M.; Berntsen, T.; DeAngelo, B.J.; Flanner, M.G.; Ghan, S.; Kärcher, B.; Koch, D.; et al. Bounding the role of black carbon in the climate system: A scientific assessment. *J. Geophys. Res. Atmos.* **2013**, *118*, 5380–5552. [CrossRef]
86. Lighty, J.S.; Veranth, J.M.; Sarofim, A.F. Combustion aerosols: Factors governing their size and composition and implications to human health. *J. Air Waste Manag. Assoc.* **2000**, *50*, 1565–1618. [CrossRef] [PubMed]
87. Jacobson, M.Z. Strong radiative heating due to the mixing state of black carbon in atmospheric aerosols. *Nature* **2001**, *409*, 695–697. [CrossRef] [PubMed]
88. Ramanathan, V.; Carmichael, G. Global and regional climate changes due to black carbon. *Nat. Geosci.* **2008**, *1*, 221–227. [CrossRef]
89. Artíñano, B.; Salvador, P.; Alonso, D.G.; Querol, X.; Alastuey, A. Influence of traffic on the PM_{10} and $PM_{2.5}$ urban aerosol fractions in Madrid (Spain). *Sci. Total Environ.* **2004**, *334–335*, 111–123. [CrossRef]
90. Clarke, A.G.; Robertson, L.A.; Hamilton, R.S.; Gorbunov, B. A Lagrangian model of the evolution of the particulate size distribution of vehicular emissions. *Sci. Total Environ.* **2004**, *334–335*, 197–206. [CrossRef]
91. Claiborn, C.S.; Finn, D.; Larson, T.V.; Koenig, J.Q. Windblown dust contributes to high $PM_{2.5}$ concentrations. *J. Air Waste Manag. Assoc.* **2000**, *50*, 1440–1445. [CrossRef]
92. Querol, X.; Alastuey, A.; Rodriguez, S.; Plana, F.; Ruiz, C.; Cots, N.; Massagué, G.; Puig, O. PM_{10} and $PM_{2.5}$ source apportionment in the Barcelona Metropolitan area, Catalonia, Spain. *Atmos. Environ.* **2001**, *35*, 6407–6419. [CrossRef]
93. Viana, M.; Querol, X.; Alastuey, A.; Gangoiti, G.; Menéndez, M. PM levels in the Basque County (Northern Spain): Analysis of a 5-year data record and interpretation of seasonal variations. *Atmos. Environ.* **2003**, *37*, 2879–2891. [CrossRef]
94. Penttinen, P.; Timonen, K.L.; Tiittanen, P.; Mirme, A.; Ruuskanen, J.; Pekkanen, J. Ultrafine particles in urban air and respiratory health among adult asthmatics. *Eur. Respir. J.* **2001**, *17*, 428–435. [CrossRef]
95. Mar, T.F.; Larson, T.V.; Stier, R.A.; Claiborn, C.; Koenig, J.Q. An analysis of the association between respiratory symptoms in subjects with asthma and daily air pollution in Spokane, Washington. *Inhal. Toxicol.* **2004**, *16*, 809–815. [CrossRef] [PubMed]
96. Siciliano, T.; De Donno, A.; Serio, F.; Genga, A. Source Apportionment of PM_{10} as a Tool for Environmental Sustainability in Three School Districts of Lecce (Apulia). *Sustainability* **2024**, *16*, 1978. [CrossRef]
97. Du, C.; Liu, S.; Yu, X.; Li, X.; Chen, C.; Peng, Y.; Dong, Y.; Dong, Z.; Wang, F. Urban boundary layer height characteristics and relationship with particulate matter mass concentrations in Xi'an, central China. *Aerosol Air Qual. Res.* **2013**, *13*, 1598–1607. [CrossRef]
98. Zhao, H.; Che, H.; Wang, Y.; Dong, Y.; Ma, Y.; Li, X.; Hong, Y.; Yang, H.; Liu, Y.; Wang, Y.; et al. Aerosol vertical distribution and typical air pollution episodes over northeastern China during 2016 analyzed by ground-based lidar. *Aerosol Air Qual. Res.* **2018**, *18*, 918–937. [CrossRef]
99. Li, X.; Ma, Y.; Wang, Y.; Wei, W.; Zhang, Y.; Liu, N.; Hong, Y. Vertical distribution of particulate matter and its relationship with planetary boundary layer structure in Shenyang, northeast China. *Aerosol Air Qual. Res.* **2019**, *19*, 2464–2476. [CrossRef]
100. Li, S.; Di, H.; Li, Y.; Yuan, Y.; Hua, D.; Wang, L.; Chen, D. Detection of aerosol mass concentration profiles using single-wavelength Raman Lidar within the planetary boundary layer. *J. Quant. Spectrosc. Radiat. Transf.* **2021**, *272*, 107833. [CrossRef]
101. Chazeau, B.; Temime-Roussel, B.; Grégory, G.; Mesbah, B.; D'Anna, B.; Wortham, H.; Marchand, N. Measurement report: Fourteen months of real-time characterization of the submicronic aerosol and its atmospheric dynamics at the Marseille-Longchamp supersite. *Atmos. Chem. Phys.* **2021**, *21*, 7293–7319. [CrossRef]
102. Lo Feudo, T.; Calidonna, C.R.; Avolio, E.; Sempreviva, A.M. Study of the Vertical Structure of the Coastal Boundary Layer Integrating Surface Measurements and Ground-Based Remote Sensing. *Sensors* **2020**, *20*, 6516. [CrossRef] [PubMed]
103. Romano, S.; Lo Feudo, T.; Calidonna, C.R.; Burlizzi, P.; Perrone, M.R. Solar eclipse of 20 March 2015 and impacts on irradiance, meteorological parameters, and aerosol properties over southern Italy. *Atmos. Res.* **2017**, *198*, 11–21. [CrossRef]
104. Federico, S.; Bellecci, C.; Colacino, M. Quantitative precipitation forecast of the Soverato flood: The role of orography and surface fluxes. *Nuovo C. Soc. Ital. Fis. C* **2003**, *26*, 7–22.
105. Federico, S.; Bellecci, C.; Colacino, M. Numerical simulation of Crotone flood: Storm evolution. *Nuovo C. Soc. Ital. Fis. C.* **2003**, *26*, 357–371.
106. Federico, S.; Avolio, E.; Bellecci, C.; Lavagnini, A.; Colacino, M.; Walko, R.L. Numerical analysis of an intense rainstorm occurred in southern Italy. *Nat. Hazards Earth Syst. Sci.* **2008**, *8*, 19–35. [CrossRef]
107. Federico, S.; Pasqualoni, L.; De Leo, L.; Bellecci, C. A study of the breeze circulation during summer and fall 2008 in Calabria, Italy. *Atmos. Res.* **2010**, *97*, 1–13. [CrossRef]
108. Federico, S.; Pasqualoni, L.; Sempreviva, A.M.; De Leo, L.; Avolio, E.; Calidonna, C.R.; Bellecci, C. The seasonal characteristics of the breeze circulation at a coastal Mediterranean site in South Italy. *Adv. Sci. Res.* **2010**, *4*, 47–56. [CrossRef]
109. Gullì, D.; Avolio, E.; Calidonna, C.R.; Lo Feudo, T.; Torcasio, R.C.; Sempreviva, A.M. Two years of wind-lidar measurements at an Italian Mediterranean Coastal Site. In European Geosciences Union General Assembly 2017, EGU—Division Energy, Resources & Environment, ERE. *Energy Procedia* **2017**, *125*, 214–220. [CrossRef]
110. Avolio, E.; Federico, S.; Miglietta, M.M.; Lo Feudo, T.; Calidonna, C.R.; Sempreviva, A.M. Sensitivity analysis of WRF model PBL schemes in simulating boundary-layer variables in southern Italy: An experimental campaign. *Atmos. Res.* **2017**, *192*, 58–71. [CrossRef]

111. Cristofanelli, P.; Busetto, M.; Calzolari, F.; Ammoscato, I.; Gullì, D.; Dinoi, A.; Calidonna, C.R.; Contini, D.; Sferlazzo, D.; Di Iorio, T.; et al. Investigation of reactive gases and methane variability in the coastal boundary layer of the central Mediterranean basin. *Elem. Sci. Anthr.* **2017**, *2017 5*, 12. [CrossRef]
112. Donateo, A.; Lo Feudo, T.; Marinoni, A.; Dinoi, A.; Avolio, E.; Merico, E.; Calidonna, C.R.; Contini, D.; Bonasoni, P. Characterization of In Situ Aerosol Optical Properties at Three Observatories in the Central Mediterranean. *Atmosphere* **2018**, *9*, 369. [CrossRef]
113. D'Amico, F.; Ammoscato, I.; Gullì, D.; Avolio, E.; Lo Feudo, T.; De Pino, M.; Cristofanelli, P.; Malacaria, L.; Parise, D.; Sinopoli, S.; et al. Integrated analysis of methane cycles and trends at the WMO/GAW station of Lamezia Terme (Calabria, Southern Italy). *Atmosphere* **2024**, *15*, 946. [CrossRef]
114. D'Amico, F.; Gullì, D.; Lo Feudo, T.; Ammoscato, I.; Avolio, E.; De Pino, M.; Cristofanelli, P.; Busetto, M.; Malacaria, L.; Parise, D.; et al. Cyclic and multi-year characterization of surface ozone at the WMO/GAW coastal station of Lamezia Terme (Calabria, Southern Italy): Implications for the local environment, cultural heritage, and human health. *Environments* **2024**, *11*, 227. [CrossRef]
115. Copernicus. Digital Elevation Model (DEM) for Europe at 30 Arc Seconds (ca. 1000 meter) Resolution Derived from Copernicus Global 30 Meter DEM Dataset. 2022. Available online: https://data.opendatascience.eu/geonetwork/srv/api/records/948c3313-9957-4581-a238-812439d44397 (accessed on 11 October 2024).
116. EMODnet Bathymetry Consortium. EMODnet Digital Bathymetry (DTM 2016). EMODnet Bathymetry Consortium. 2016. Available online: https://sextant.ifremer.fr/record/c7b53704-999d-4721-b1a3-04ec60c87238/ (accessed on 30 September 2024).
117. D'Amico, F.; Ammoscato, I.; Gullì, D.; Avolio, E.; Lo Feudo, T.; De Pino, M.; Cristofanelli, P.; Malacaria, L.; Parise, D.; Sinopoli, S.; et al. Trends in CO, CO_2, CH_4, BC, and NO_x during the first 2020 COVID-19 lockdown: Source insights from the WMO/GAW station of Lamezia Terme (Calabria, Southern Italy). *Sustainability* **2024**, *16*, 8229. [CrossRef]
118. Italian Republic. Decree of the President of the Council of Ministers, 9 March 2020. GU Serie Generale n. 62. Available online: https://www.gazzettaufficiale.it/eli/id/2020/03/09/20A01558/sg (accessed on 9 October 2024).
119. Donateo, A.; Lo Feudo, T.; Marinoni, A.; Calidonna, C.R.; Contini, D.; Bonasoni, P. Long-term observations of aerosol optical properties at three GAW regional sites in the Central Mediterranean. *Atmos. Res.* **2020**, *241*, 104976. [CrossRef]
120. D'Amico, F.; Ammoscato, I.; Gullì, D.; Avolio, E.; Lo Feudo, T.; De Pino, M.; Cristofanelli, P.; Malacaria, L.; Parise, D.; Sinopoli, S.; et al. Anthropic-induced variability of greenhouse gases and aerosols at the WMO/GAW coastal site of Lamezia Terme (Calabria, Southern Italy): Towards a new method to assess the weekly distribution of gathered data. *Sustainability* **2024**, *16*, 8175. [CrossRef]
121. Calidonna, C.R.; Avolio, E.; Gullì, D.; Ammoscato, I.; De Pino, M.; Donateo, A.; Lo Feudo, T. Five Years of Dust Episodes at the Southern Italy GAW Regional Coastal Mediterranean Observatory: Multisensors and Modeling Analysis. *Atmosphere* **2020**, *11*, 456. [CrossRef]
122. Malacaria, L.; Parise, D.; Lo Feudo, T.; Avolio, E.; Ammoscato, I.; Gullì, D.; Sinopoli, S.; Cristofanelli, P.; De Pino, M.; D'Amico, F.; et al. Multiparameter detection of summer open fire emissions: The case study of GAW regional observatory of Lamezia Terme (Southern Italy). *Fire* **2024**, *7*, 198. [CrossRef]
123. JIN, Y.; Sugimoto, N.; Shimizu, A.; Nishizawa, T.; Kai, K.; Kawai, K.; Yamazaki, A.; Sakurai, M.; Wille, H. Evaluation of ceilometer attenuated backscattering coefficients for aerosol profile measurement. *J. Appl. Remote Sens.* **2018**, *12*, 042604. [CrossRef]
124. Tyagi, S.; Tiwari, S.; Mishra, A.; Singh, S.; Hopke, P.K.; Singh, S.; Attri, S.D. Characteristics of absorbing aerosols during winter foggy period over the National Capital Region of Delhi: Impact of planetary boundary layer dynamics and solar radiation flux. *Atmos. Res.* **2017**, *188*, 1–10. [CrossRef]
125. Seibert, P.; Beyrich, F.; Gryning, S.-E.; Joffre, S.; Rasmussen, A.; Tercier, P. Review and intercomparison of operational methods for the determination of the mixing height. *Atmos. Environ.* **2000**, *34*, 1001–1027. [CrossRef]
126. G. Lufft Mess. *Manual Ceilometer CHM 15k "NIMBUS"*; Campbell Scientific: Edmonton, AB, Canada, 2016.
127. Philipona, R.; Kräuchi, A.; Brocard, E. Solar and thermal radiation profiles and radiative forcing measured through the atmosphere. *Geophys. Res. Lett.* **2012**, *39*, L13806. [CrossRef]
128. Lo Feudo, T.; Avolio, E.; Gullì, D.; Federico, S.; Calidonna, C.R.; Sempreviva, A. Comparison of Hourly Solar Radiation from a Ground-Based Station, Remote Sensing and Weather Forecast Models at a Coastal Site of South Italy (Lamezia Terme). *Energy Procedia* **2015**, *76*, 148–155. [CrossRef]
129. Chu, P.M.; Hodges, J.T.; Rhoderick, G.C.; Lisak, D.; Travis, J.C. Methane-In-Air Standards Measured Using a 1.65 Mm Frequency-Stabilized Cavity Ring-Down Spectrometer. In *Proc SPIE 6378, Chemical and Biological Sensors for Industrial and Environmental Monitoring II*; The International Society for Optical Engineering: Bellingham, WA, USA, 2006; p. 63780G. [CrossRef]
130. Petzold, A.; Kramer, H.; Schönlinner, M. Continuous Measurement of Atmospheric Black Carbon Using a Multi-angle Absorption Photometer. *Environ. Sci. Pollut. Res.* **2002**, *4*, 78–82.
131. Petzold, A.; Schönlinner, M. Multi-angle absorption photometry—A new method for the measurement of aerosol light absorption and atmospheric black carbon. *J. Aerosol Sci.* **2004**, *35*, 421–441. [CrossRef]
132. Petzold, A.; Schloesser, H.; Sheridan, P.J.; Arnott, P.; Ogren, J.A.; Virkkula, A. Evaluation of multiangle absorption photometry for measuring aerosol light absorption. *Aerosol Sci. Technol.* **2005**, *39*, 40–51. [CrossRef]
133. Müller, T.; Henzing, J.S.; de Leeuw, G.; Wiedensohler, A. Design and performance of a three-wavelength LED-based total scatter and backscatter integrating nephelometer. *Atmos. Meas. Tech.* **2011**, *4*, 1291–1303. [CrossRef]

134. Carslaw, D.C.; Ropkins, K. Openair—An R package for air quality data analysis. *Environ. Model. Softw.* **2012**, *27–28*, 52–61. [CrossRef]
135. Carslaw, D.C. *The Openair Manual—Open-Source Tools for Analysing Air Pollution Data. Manual for Version 2.6-6*; University of York: Heslington, UK, 2019.
136. Tsaknakis, G.; Papayannis, A.; Kokkalis, P.; Amiridis, V.; Kambezidis, H.D.; Mamouri, R.E.; Georgoussis, G.; Avdikos, G. Inter-comparison of lidar and ceilometer retrievals for aerosol and Planetary Boundary Layer profiling over Athens, Greece. *Atmos. Meas. Tech. Discuss.* **2011**, *4*, 73–99. [CrossRef]
137. Fan, J.; Shao, L.; Hu, Y.; Wang, J.; Wang, J.; Ma, J. Classification and chemical compositions of individual particles at an eastern marginal site of Tibetan Plateau. *Atmos. Pollut. Res.* **2016**, *7*, 833–842. [CrossRef]
138. Witte, A.; Garg, N. Particle shape, crystallinity, and degree of polymerization of fly ash via combined SEM-EDS and Raman spectroscopy. *Cem. Concr. Res.* **2024**, *184*, 107612. [CrossRef]
139. Luo, H.; Han, Y.; Lu, C.; Yang, J.; Wu, Y. Characteristics of Surface Solar Radiation under Different Air Pollution Conditions over Nanjing, China: Observation and Simulation. *Adv. Atmos. Sci.* **2019**, *36*, 1047–1059. [CrossRef]
140. Ricaud, P.; Sič, B.; El Amraoui, L.; Attié, J.-L.; Zbinden, R.; Huszar, P.; Szopa, S.; Parmentier, J.; Jaidan, N.; Michou, M.; et al. Impact of the Asian monsoon anticyclone on the variability of mid-to-upper tropospheric methane above the Mediterranean Basin. *Atmos. Chem. Phys.* **2014**, *14*, 11427–11446. [CrossRef]
141. Gerasopoulos, E.; Kouvarakis, G.; Vrekoussis, M.; Donoussis, C.; Mihalopoulos, N.; Kanakidou, M. Photochemical ozone production in the Eastern Mediterranean. *Atmos. Environ.* **2006**, *40*, 3057–3069. [CrossRef]
142. Kalabokas, P.D.; Mihalopoulos, N.; Ellul, R.; Kleanthous, S.; Repapis, C.C. An investigation of the meteorological and photochemical factors influencing the background rural and marine surface ozone levels in the Central and Eastern Mediterranean. *Atmos. Environ.* **2008**, *42*, 7894–7906. [CrossRef]